



Contents lists available at ScienceDirect

## Journal of Nuclear Materials

journal homepage: [www.elsevier.com/locate/jnucmat](http://www.elsevier.com/locate/jnucmat)

# On the feasibility to obtain CuCrZr alloys with outstanding thermal and mechanical properties by additive manufacturing

F. Canillas<sup>a,\*</sup>, E. Leon-Gutierrez<sup>a</sup>, M. Roldan<sup>a</sup>, R. Hernandez<sup>b</sup>, E. Urionabarrenetxea<sup>c</sup>,  
E. Cardozo<sup>c</sup>, L. Portoles<sup>d</sup>, J.R. Blasco<sup>d</sup>, N. Ordas<sup>c</sup>

<sup>a</sup> National Fusion Laboratory, CIEMAT, Madrid 28040, Spain

<sup>b</sup> Energy Interest Materials Division, CIEMAT, Madrid 28040, Spain

<sup>c</sup> Ceit-BRTA and Tecnun (Universidad de Navarra), Donostia-San Sebastián 20018, Spain

<sup>d</sup> AIDIMME, Leonardo da Vinci 38, Paterna 46980, Spain

## HIGHLIGHTS

- Additive manufacturing of High Heat Flux materials for nuclear fusion applications.
- EB-PBF CuCrZr manufacturing with outstanding mechanical and thermal properties.
- Hierarchical microstructure on additively manufactured CuCrZr.
- Advanced microstructural and mechanical characterization of CuCrZr.
- Characterization of additively manufactured CuCrZr for nuclear fusion divertor.

## ARTICLE INFO

### Keywords:

Additive manufacturing  
High Heat Flux components  
CuCrZr  
Electron beam powder  
Bed Fusion (EB-PBF)  
Nuclear fusion  
Cu alloys characterization

## ABSTRACT

The CuCrZr alloy combines high thermal conductivity and mechanical strength with stability at high-medium temperatures, making it a promising heat sink material for the EU-DEMO divertor and limiters. Additive Manufacturing (AM) technologies have proven effective in developing complex-shaped components with almost no constraints on geometry and minimal machining and welding requirements. This makes them particularly suitable for the production of heat exchangers featuring complex cooling channels with intricate inner structures.

This study demonstrates the feasibility to obtain dense CuCrZr via Electron Beam Powder Bed Fusion (EB-PBF) with high thermal conductivity and enhanced mechanical strength compared to conventional routes. Gas atomization was used to produce spherical powders with a composition close to ITER specifications. By optimising the EB-PBF process parameters, relative density values of 99.7 % were achieved after HIP treatment, that removes the eventual residual porosity. The results underscore the importance of meticulous powder manufacturing to mitigate oxidation and microstructural defects in the final components. Achieving high relative densities in the EB-PBF process requires a focus on adopting high-energy absorption rates in the powders. This strategy can be accomplished by reducing the scanning speed and consequently the building rate of the process. The microstructural characterization revealed a complex hierarchical microstructure composed of grains and grain boundaries, solidification-enabled cellular-like subgrains elongated along the building direction and an ultra-fine precipitate state (already present in the as-built condition) mainly consisting of Cr-rich nano-precipitates, although Zr-rich precipitates were also found at the melt pool boundaries. The thermal conductivity, hardness, mechanical strength at room temperature and high-medium temperatures were measured and correlated with the EB-PBF process parameters and the microstructure obtained after HIP treatment. The results indicate that it is possible to obtain CuCrZr with improved mechanical behaviour compared to conventional manufacturing technologies, while maintaining the thermal conductivity requirements for EU-DEMO.

\* Corresponding author.

E-mail address: [franciscoj.canillas@ciemat.es](mailto:franciscoj.canillas@ciemat.es) (F. Canillas).

<https://doi.org/10.1016/j.jnucmat.2024.155304>

Received 22 April 2024; Received in revised form 19 July 2024; Accepted 25 July 2024

Available online 28 July 2024

0022-3115/© 2024 The Authors. Published by Elsevier B.V. This is an open access article under the CC BY-NC license (<http://creativecommons.org/licenses/by-nc/4.0/>).

## 1. Introduction

Efforts to harness energy from controlled nuclear fusion reactions are at the forefront of current research endeavours. High Heat Flux (HHF) and Plasma-Facing components (PFCs) in the divertor and limiters will play a key role of the configuration of ITER and the future EU-DEMO nuclear fusion reactors. The plasma-facing materials (PFMs) of these components shall withstand extremely heavy thermal shocks under both normal operating conditions and during transient or off-normal events, mainly controlled by the divertor and the limiters, respectively. For example, the EU-DEMO divertor will be subjected to a heat flux ranging from 1 to 20 MW/m<sup>2</sup>, depending on the specific component of the divertor impinged [1], while its limiters will bear similar values of 5–20 MW/m<sup>2</sup> when talking about the Outboard and Inboard Mid-plane Limiters (OML and IML, respectively), but more extreme situations could happen in the Upper Limiter (UL, ~25 GW/m<sup>2</sup>) or in the Outboard Lower Limiter (OLL, ~150 GW/m<sup>2</sup>) [2]. Therefore, a comprehensive search of materials and alloys suitable for this purpose is underway.

CuCrZr, a precipitation-hardened alloy, currently stands as one of the main candidates to be used as heat sink material in these components [1–4]. For these applications, demanding criteria including very high thermal conductivity and reasonably high mechanical strength are essential, as the heat sink is required not only to facilitate heat dissipation but also to provide vital structural support [1]. In this scenario, the use of a Cu alloy rather than pure Cu as a heat sink is crucial, considering that pure Cu, being excessively ductile, may not meet the required mechanical strength. The ITER Material Property Handbook (MPH) defines the composition of the ITER grade of CuCrZr (CuCrZr-IG) as follows: 0.6–0.9 wt.% Cr - 0.07–0.15 wt.% Zr - Bal. wt.% Cu [4,5]. The Cr limits aim to achieve a final microstructure with a homogeneous distribution of ultra-fine Cr-rich precipitates, which is critical for a precipitation-hardened alloy [6]. Meanwhile, the Zr limits are required to control grain size, improve fatigue and creep resistance, and prevent welding-related defects during assembly of reactor components.

CuCrZr can satisfactorily meet functional and mechanical ITER requirements if the appropriate post-build heat treatments are applied, and is the primary contender for HHF and PFCs in the EU-DEMO divertor [4,7]. As a precipitation-hardened alloy, this material can reach several condition depending on the heat treatment applied, which were collected in the ITER Plant Description document [8]. SAA and SACwA are frequently cited heat treatments in the literature [9–11]:

- **SAA** – Solution annealing at 980–1000 °C for 30–60 min, followed by water quenching and ageing at 460–500 °C for 2–4 h.
- **SACwA** – Solution annealing at 980–1000 °C for 30–60 min, subsequent cooling in water, further cold working by 40–70 %, and ageing at 450–470 °C for 2–4 h.

However, they have not been formally established as the standard heat treatments for CuCrZr. This is because ongoing research continues to explore the influence of various parameters within these processes on the resulting mechanical properties, which warrants further investigation. The main objective of these treatments is directly related to the Cr content specified for the ITER grade of this alloy: to obtain an ultra-fine precipitation state of Cr-rich particles, homogeneously distributed. Achieving such microstructure requires obtaining a supersaturated solid solution of Cr in Cu through solution annealing followed by rapid gas cooling or water quenching (minimum cooling rates approx. >1.5 °C/sec [12]). Subsequently, aging treatment promotes the decomposition of this solid solution, where the driving force for the reaction is the large difference in the solid solubility of Cr in Cu near the eutectic temperature (0.73 wt.%, at 1077 °C) and during ageing at 475 °C (0.10 wt.%) [13]. It is noteworthy that previous research has concluded that the optimal temperature for ageing is 475 °C for 3 h, supported by electrical resistivity and hardness measurements [14,15]. In the case of SACwA heat treatment, a 40–70 % cold working process is carried out prior to

ageing to improve mechanical properties [11].

The ITER mechanical and thermal requirements for the CuCrZr alloy are specified in the Appendix A to the Structural Design Criteria for ITER In-vessel Components (SDC-IC) [16]. Within this document, average and minimum properties are provided for both the SAA and SACwA conditions, as well as the ITER-oriented minimum properties required for this alloy, considering any degradation due to manufacturing thermal cycles during the assembly of the reactor modules. These mechanical and thermal properties are summarized in Table 1, where only minimum values have been reported for the SACwA condition, while the properties indicated for the SAA represent average values. The properties are given for 20 (room temperature, RT), 250 and 350 °C, as the maximum service temperature for CuCrZr when operated under neutron irradiation is 350 °C, according to the design criteria followed to date [7]. The ITER-oriented minimum properties are labelled as "ITER requirements" in Table 1 and the reported data demonstrates that this alloy meets these criteria. However, it is important to note that the specifications for the EU-DEMO reactor and future higher power reactors will likely be more demanding [17].

Advanced manufacturing technologies such as additive manufacturing (AM) have attracted a great deal of interest in the production of Cu and Cu alloys in recent years. The almost unlimited freedom to produce complex geometries that AM offers makes it an interesting candidate process for the manufacture of heat exchangers with complex internal cooling channels and high surface-to-volume ratio [18,19]. In addition, AM offers the advantage of reducing the need for welding operations that could damage the appropriate microstructure and, hence, the mechanical properties obtained after applying the heat treatments optimised for this alloy [20–22]. This reduction in welding operations is particularly important as the high temperatures involved in welding can negatively affect the microstructure and the properties achieved through prior heat treatments. Furthermore, AM allows for greater efficiency in the utilization of raw materials. By enabling the production of near-net shape components, AM significantly reduces the need for extensive machining and minimizes material waste. This is particularly beneficial in industries like nuclear energy, where a large number of complex and specific components are required for the continued operation of reactors. With AM, almost any component can be produced on-demand, provided that the raw material with the correct composition is available. This capability reduces the need for large inventories of spare parts, as components can be manufactured as needed. To be useful, materials produced by AM must meet the minimum requirements set for ITER grade, just like conventional manufacturing methods listed earlier.

Moreover, Powder Bed Fusion (PBF) AM technologies offer an exceptional added benefit in the production of precipitation-hardened alloys. These processes rely on the rapid melting and subsequent solidification of the metal powder bed with the desired composition using laser or electron beams, resulting in a microstructure of ultra-fine precipitates even in the as-built condition. In particular, laser-based PBF (L-PBF) has been widely employed to produce CuCrZr components. However, significant efforts have been required to optimise the L-PBF scanning process parameters in order to avoid lack of fusion or delamination defects correlated with the high reflectivity and high thermal conductivity of Cu and Cu alloys, and to attain high relative density values [23–27]. Recent advances in blue or green diode laser sources have proven effective in increasing energy absorption during the fusion process of the powders, reducing reflectivity to 40 % [28].

Given these challenges, opting for an electron beam rather than a laser beam seems to be a reasonable alternative to mitigate the issue of low energy absorption, in order to prevent delamination defects and porosity derived from lack of fusion of the metal powder bed. Electron Beam Powder Bed Fusion (EB-PBF, also named Electron Beam Melting, EBM) has already demonstrated its capability in producing pure Cu parts with remarkable outcomes, achieving high relative densities of over 99.9 % [29,30]. However, except for our recent work [31], there is a

**Table 1**

ITER-oriented minimum properties (ITER requirements) for CuCrZr-ITER Grade. In addition, the average properties for SAA (Solution Annealed and Aged) CuCrZr, and the minimum properties for SACwA (Solution Annealed, cold worked and Aged) CuCrZr are provided. The Young's modulus values, thermal conductivity and hardness values are also included [16]. (NR: Not reported).

	ITER requirements			SAA CuCrZr (average values)			SACwA CuCrZr (minimum values)		
	20 °C	250 °C	350 °C	20 °C	250 °C	350 °C	20 °C	250 °C	350 °C
UTS (MPa)	280	220	194	405	315	274	452	342	307
Rp (MPa)	175	150	139	287	244	217	407	331	294
UE (%)	NR	NR	NR	18.4	13.7	13.2	5.9	1.1	0
TE (%)	NR	NR	NR	27.0	21.0	23.0	10.0	1.1	0
E <sup>i</sup> (GPa)	NR	NR	NR	125	117	110	127	115	110
$\lambda^{\text{II}}$ (W/(m•K))	325/355	345/355	345/355	318	345	347	318	345	347
HV0.5 <sup>III</sup>	126	–	–	–	–	–	–	–	–

i. Young's modulus values are referenced to the ITER MPH of CuCrZr [4].

ii. ITER thermal conductivity requirement varies depending on design criteria (ITER Document No. G74 MA16 [56] vs. ITER Document No. S74 MA2 [57]).

iii. Hardness value recommendation for CuCrZr-ITER grade is referenced to [41].

lack of previous research on the fabrication of the CuCrZr alloy using the EB-PBF technique. In this work, a first approach to optimise the EB-PBF fabrication process parameters to obtain nearly fully dense CuCrZr parts (up to 99.8 %) was performed. Hardness values above ITER recommendations were obtained, even in the as-built state. A homogeneous distribution of Cr-rich precipitates was obtained and no significant differences in this distribution were observed between the as-built condition and the heat-treated specimens.

Building on the findings of our previous work [31], this study demonstrates the repeatability in the fabrication of highly densified CuCrZr-ITER grade specimens via EB-PBF, with further optimisation of the fabrication process parameters. The microstructure, mechanical properties and thermal conductivity were analysed after a Hot Isostatic Pressing (HIP) treatment and correlated with the fabrication parameters.

## 2. Experimental and methodology

Gas-atomized CuCrZr powders with two different compositions were used (Table 2, designated CuCrZr-TLS and CuCrZr-3). The compositions CuCrZr-1 and CuCrZr-2 were previously introduced in [31]. CuCrZr-TLS represents commercial powders purchased from Eckart TLS, Germany, and produced using an EIGA atomizer. CuCrZr-3 was obtained at the research centre Ceit, Spain, using a PSI Hermiga 75/3 VIGA close-coupled gas atomizer. The powders were sieved to 45–106  $\mu\text{m}$  and the resulting particle size distribution (PSD), measured by dynamic image analysis, is given in Table 3. Fig. 1 shows FE-SEM micrographs of the powders from both the CuCrZr-TLS and CuCrZr-3 batches. Two EB-PBF fabrications, named EBM-TLS and EBM3 (EBM refers to Electron Beam Melting), were produced using the CuCrZr-TLS and CuCrZr-3 powder batches, respectively, at the research centre Aidimme, Spain, in an Arcam A2X EB-PBF system. Each batch maintains the composition of the corresponding powder batch used. The initial EB-PBF fabrication process parameters were selected from the best results obtained in our previous work [31] (Table 4). In both fabrications (EBM-TLS & EBM3), the layer thickness was set to 70  $\mu\text{m}$ , the scan pattern followed by the electron beams was rotated 90° with each layer, and the whole process was performed under vacuum with a low partial pressure of He ( $2 \cdot 10^{-3}$  mbar). The powder bed temperature was controlled by

**Table 2**

Composition of the gas-atomized powders used in EB-PBF manufacturing. Impurity concentrations measured for the powder atomized at Ceit (CuCrZr-3) are included, while details regarding impurity concentrations of CuCrZr-TLS have been supplied by Eckart TLS.

Batch code	Composition (wt.%)			Impurities (ppm weight)							
	Cu	Cr	Zr	O	C	N	S	B	Al	Si	Fe
CuCrZr-TLS	Bal.	0.74	0.12	269	–	–	–	–	<2000	≤1000	≤800
CuCrZr-3	Bal.	0.95	0.063	21–113	27	2	3	7	<200	130	120

**Table 3**

Particle size distribution (PSD) of the gas-atomized powders used in the EB-PBF manufacturing.

Batch code	PSD ( $\mu\text{m}$ )		
	D10	D50	D90
CuCrZr-TLS	51	70	97
CuCrZr-3	51	73	103

thermocouples located beneath the platform table of the EB-PBF system. However, due to technical constraints, direct measurement of the powder bed temperature is extremely challenging. The platform was set to 380 °C, considering that the actual temperature of the powders would be slightly higher due to pre-heating scans before each powder layer is melted. Additionally, within the EBM3 batch, sub-batches labelled as EBM3.1, EBM3.2 and EBM3.3 were fabricated to explore modifications in the main EB-PBF process parameters, as detailed in Table 4. These adjustments aimed to optimize various parameters such as scanning speed, beam current, and line offset. The primary objective was to increase the building rate for faster printing while also investigating how the absorbed energy affects the final density of the fabricated part. Subsequently, based on the knowledge acquired, EBM3.4 was produced to machine the mechanical test samples. Fig. 2 displays EBM-TLS and EBM3.4, which have also meant an increase in the size and complexity of the parts manufactured by EB-PBF. A post-build Hot Isostatic Pressing process (HIP, 450 °C, 150 MPa, 3 h) was applied to remove the eventual residual porosity. A post-build Hot Isostatic Pressing process (HIP, 450 °C, 150 MPa, 3 h) was applied to remove the eventual residual porosity. Unlike conventional powder metallurgy where HIP processes require encapsulating the raw material, in additive manufacturing, the final-shaped part can be directly subjected to HIP. This is feasible as long as there are no surface pores interconnected with the interior of the material, which could otherwise destabilize the process. This advantage significantly simplifies the HIP treatment in AM, making it a more practical and efficient option for producing complex geometries.

Density measurements at RT were performed using the Archimedes method [32], in the as-built condition and after HIP. The microstructures were analysed by optical microscopy (OM) and Field Emission

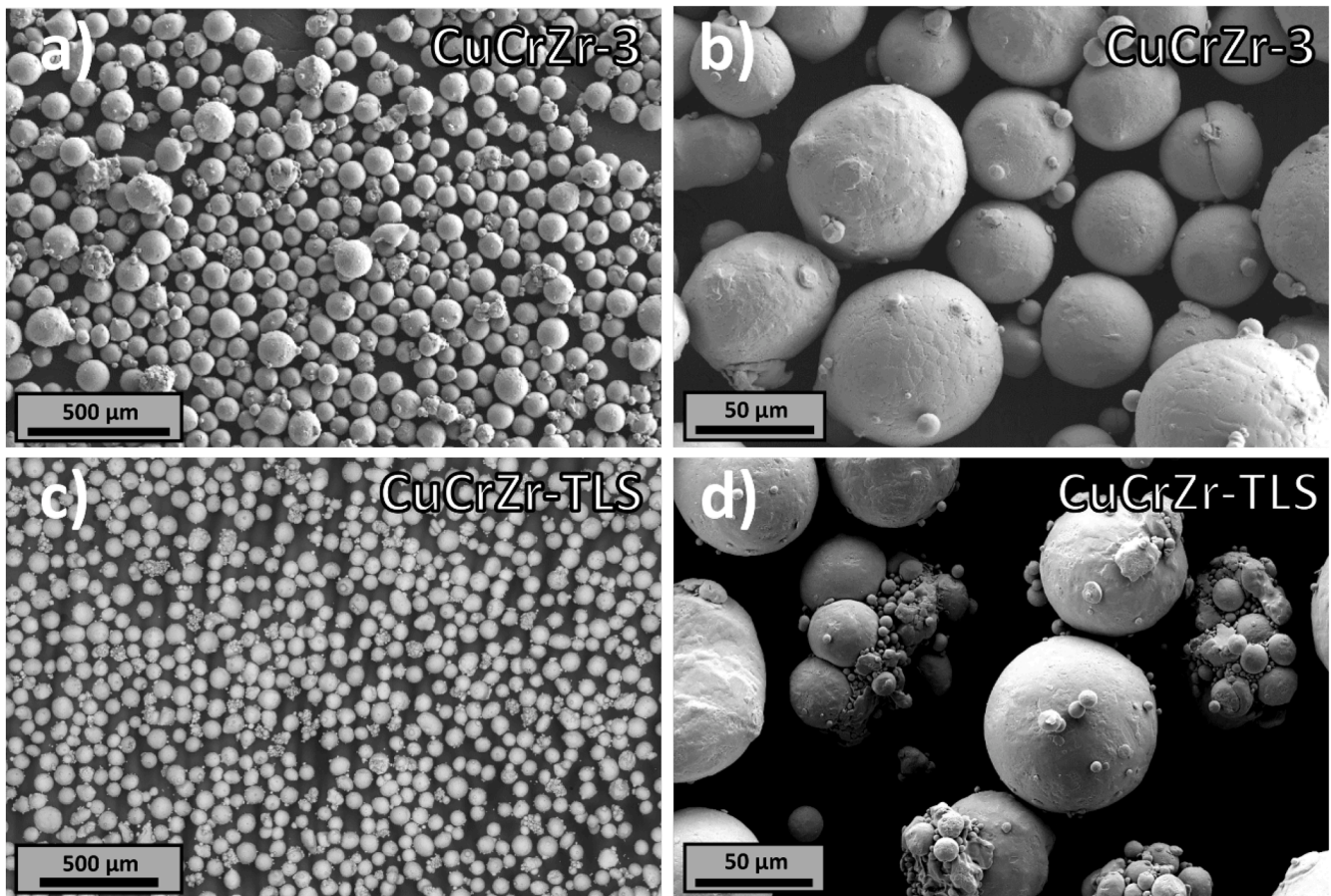


Fig. 1. FE-SEM micrograph of the gas-atomized powders: (a) and (b) CuCrZr-3; (c) and (d) CuCrZr-TLS. (45–106  $\mu\text{m}$ ).

Table 4

EB-PBF fabrication process parameters for each EB-PBF batch.

EB-PBF fabrication process parameters							
EB-PBF fabrication	Energy (J/mm <sup>2</sup> )	Beam Current (mA)	Scanning Speed (mm/s)	Line offset (mm)	Focus offset (mA)	Layer thickness ( $\mu\text{m}$ )	Powder bed temperature ( $^{\circ}\text{C}$ )
EBM-TLS	8.7	8	550	0.10	15	70	> 380
EBM3.1	8.7–14.4	12	500–826	0.10	15	70	> 380
EBM3.2	5.8–10.1	10	593–1028	0.10	15	70	> 380
EBM3.3	5.0–13.5	6–12	300–582	0.10–0.19	15	70	> 380
EBM3.4	30.5	8.5	170	0.15	22	70	> 380

Scanning Electron Microscopy (FE-SEM) equipped with an Energy Dispersive X-Ray Spectrometer (EDS). The fine Cr- and Zr-rich precipitates were examined in detail using Transmission Electron Microscopy (TEM) equipped with an EDS. Two methods were followed to prepare thin specimens suitable for TEM analysis: the conventional thin foil method and the carbon extraction replica technique [33]. Furthermore, thermal conductivity was measured using the Laser Flash Method (MicroFlash® 457, Netzsch) on samples with dimensions of  $10,0 \times 10,0 \times 2,0$  mm.

Mechanical properties were measured through tensile testing, Charpy impact testing and hardness measurements. Tensile tests were performed at room and high-medium temperatures (250 and 350  $^{\circ}\text{C}$ ) in air, using a strain rate of  $1 \text{ min}^{-1}$ , on a servo-hydraulic universal testing machine equipped with a radiant furnace. Engineering stress-strain curves were obtained following the ASTM standards E8E8M-21 and E21 [34,35]. Round specimens of various sizes were machined from EBM-TLS and EBM3.4, with the tensile axis perpendicular to the building direction (BD), as indicated in Fig. 3a and 3b. Due to limitations in

the availability of material, the size of the EBM-TLS mechanical samples was reduced. This adjustment was made as a result of the finite quantity of commercial powder (CuCrZr-TLS) acquired for this initial screening phase. Fracture surfaces were analysed by means of electron microscopy in order to clarify the nature of the fracture. According to the ITER MPH of CuCrZr [4], direct determination of the Young's modulus from the stress-strain curves is not valid due to the low accuracy of this method. Instead, this property should be obtained through sonic measurements, namely dynamic methods. The Impulse Excitation Technique was employed to determine the Young's modulus of EBM3.4 specimens at RT. Again, EBM-TLS specimens for Young's modulus measurement could not be obtained due to limitations of the material available. This circumstance arose due to the finite quantity of commercial powder acquired for this particular phase of the study. Charpy impact tests were performed at RT on a Zwick/Roell HIT 25/50P impact tester. Impact tests at the operational temperature range (250  $^{\circ}\text{C}$  / 350  $^{\circ}\text{C}$  [7]) of this alloy could not be conducted due to limitations in material availability. Miniaturized Charpy V-notch specimens from EBM-TLS and EBM3.4

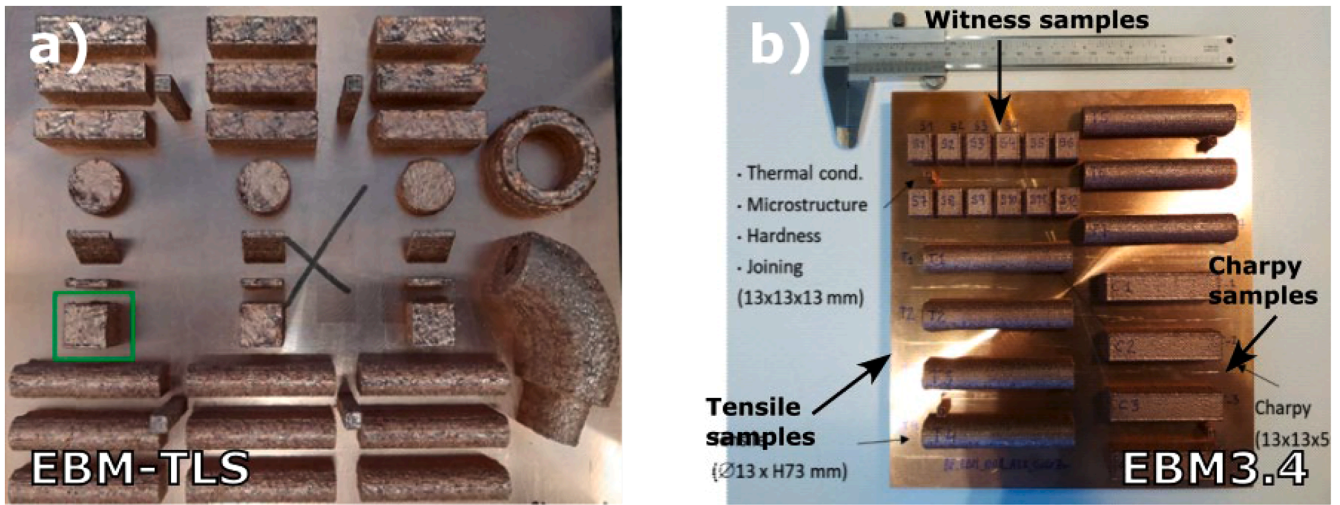


Fig. 2. EB-PBF fabrications: (a) EBM-TLS and (b) EBM3.4.

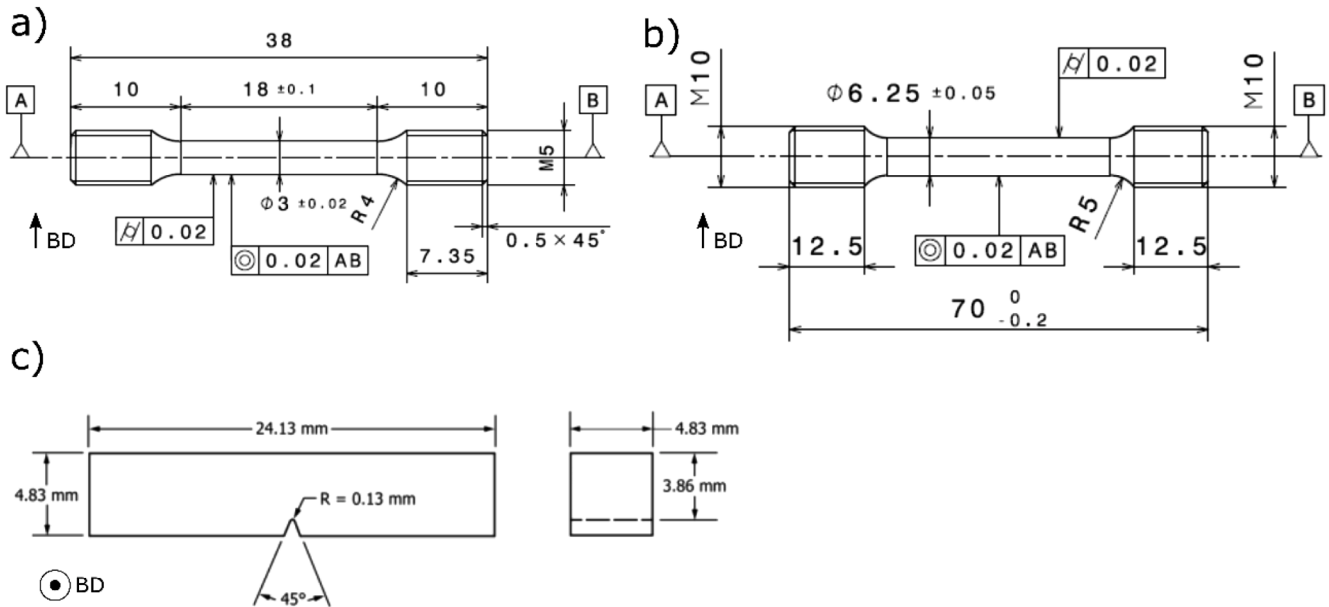


Fig. 3. Schematic drawing of mechanical specimens (Dimensions in mm; BD: Building Direction): (a) Smallest tensile specimens used for EBM-TLS testing, due to limitations in the available material; (b) Standard tensile specimens used for EBM3.4 testing; (c) Miniaturized Charpy V-notch specimens used for EBM-TLS and EBM3.4 Charpy testing.

batches were machined according to the ASTM Standard E2248–18 (Fig. 3c). This limitation is caused by the laboratory scale of our research, but does not suggest a scalability issue; rather, it reflects the finite quantity of commercial CuCrZr-TLS powders acquired and the limited production of CuCrZr-3 powders via gas-atomization for this research. That is, it underscores that we were operating within a laboratory-scale phase. Orientation of the notch was set perpendicular to the building direction. Vickers microhardness tests were conducted with a load of 500 gf for 14 s, and the samples were prepared through conventional grinding and polishing down to 0.25  $\mu\text{m}$  particle size.

### 3. Results

#### 3.1. Gas atomization

Gas-atomized CuCrZr-3 powder has shown significant improvements in powder manufacturing practices, drawing upon insights from our

previous study [31]. Fig. 1a and 1b show a low presence of satellites and agglomerates. In contrast, the morphology of CuCrZr-TLS commercial powder exhibited a high density of satellites and agglomerates (Fig. 1c and 1d). The internal microstructure of CuCrZr-3 (Fig. 4) consists of fine equiaxed grains with precipitates along grain boundaries, reported in our previous study [31] as Cr-rich and Zr-rich precipitates. The particle size distribution ranges from 45 to 106  $\mu\text{m}$ , following a lognormal distribution characterized by parameters:  $D[4,3]=73.5 \mu\text{m}$ ,  $D10=51 \mu\text{m}$ ,  $D50=73 \mu\text{m}$ , and  $D90=103 \mu\text{m}$ . Table 1 shows the impurity concentrations, where it is worth emphasizing the low levels of oxygen and aluminium achieved.

#### 3.2. Relative density and thermal conductivity measurements

The relative density ( $\rho_{rel}$ ) results varied among the initial EB-PBF batches fabricated (EBM-TLS, EBM3.1, EBM3.2 & EBM3.3), with an average value hovering around 95 % (porosity  $\leq 5$  %). However, optical

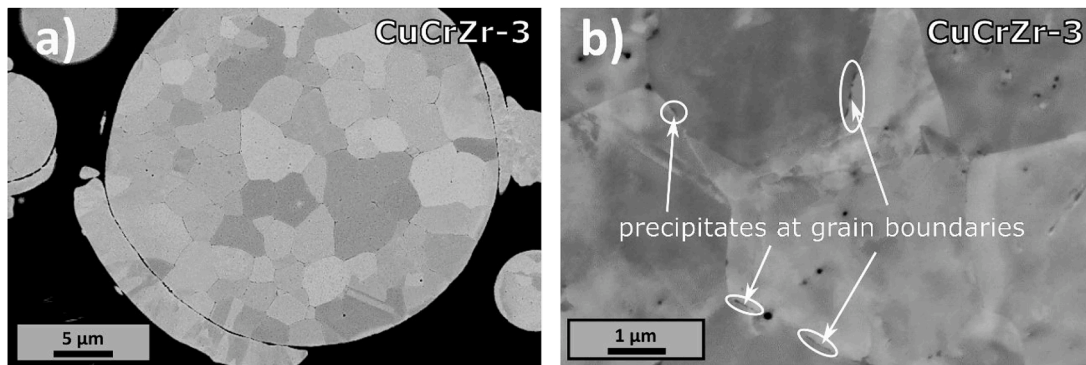


Fig. 4. FE-SEM micrograph of the CuCrZr-3 gas-atomized powders (internal microstructure). Cr-rich and Zr-rich precipitates at grain boundaries are indicated in (b).

microscopy revealed significant differences in the nature of the porosity obtained in each batch: EBM-TLS, EBM3.2, and EBM3.3 showed a non-homogeneous distribution of pores with irregular shape and frequent interconnections. This porosity is often related to powder's lack of fusion, and depends not only on the EB-PBF fabrication process parameters, but also on other factors such as the composition or quality of the powders (the degree of oxidation, morphology, size and density of agglomerates and satellites). In contrast, EBM3.1, which corresponds to the highest energy absorption per square millimetre (Table 4), exhibited a homogeneous distribution of spherical and individual pores. These characteristics are illustrated in Fig. 5.

Based on this initial results, EBM3.4 was manufactured with a set of EB-PBF fabrication process parameters aimed at increasing the energy absorbed by the powders during manufacturing, which was mainly

achieved by significantly decreasing the scanning speed of the EB-PBF process. The porosity in this batch was only reduced down to 3 %; however, the resulting pores were predominantly spherical and isolated (Fig. 5), indicating an improvement in pore morphology compared to previous batches such as EBM-TLS, EBM3.2, and EBM3.3. All the batches were subsequently subjected to a HIP treatment (450 °C, 150 MPa, 3 h). However, only specimens from EBM3.1 and EBM3.4 exhibited reductions in residual porosity after HIP, achieving average  $\rho_{rel}$  values of 99.7 %  $\pm$  0.2 % and 99.5 %  $\pm$  0.1 %, respectively. A quantitative analysis was performed on EBM3.4 specimens after HIP, obtaining average porosity size values of about 20  $\pm$  6 μm, generally not exceeding 60 μm as maximum size. Regarding thermal conductivity, only specimens with high relative density met ITER specifications (see data in Table 1). The thermal conductivity results for EBM3.4 yielded promising

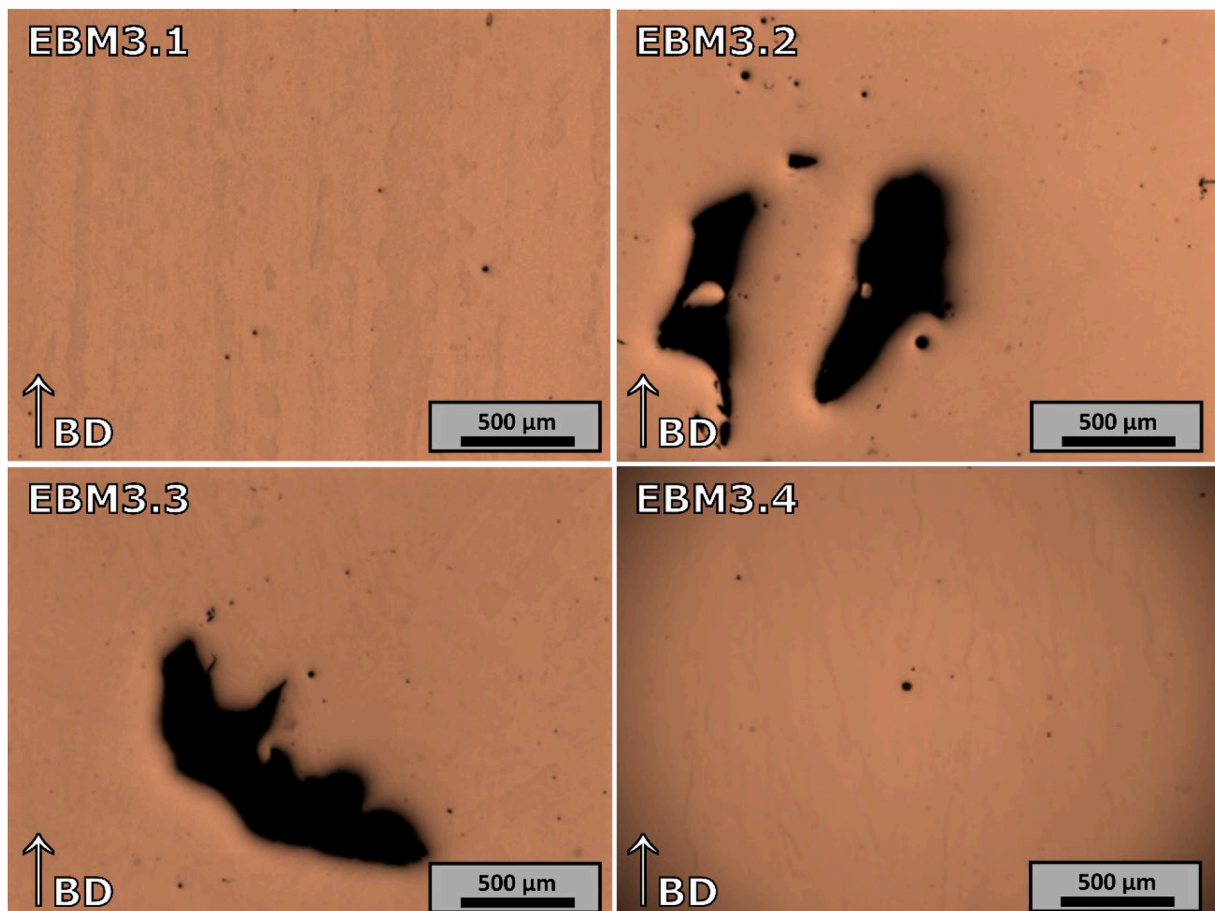


Fig. 5. OM micrographs showing the morphology, size and distribution of the porosity of the EB-PBF fabrications, in the as-built condition (BD: Building Direction).

outcomes, ranging from 345 to 360 W/m•K. Unfortunately, as mentioned before, limitations in material availability from the EBM3.1 batch rendered the production of suitable specimens for thermal conductivity measurements impossible.

### 3.3. Microstructural characterization before and after HIP treatment

The microstructure of both the as-built and the HIPped specimens showed the same typical features of materials produced by PBF additive manufacturing technologies: elongated zigzag Cu grains aligned parallel to the building direction [24,25,27,30,31,36–38]. The chemically etched surface of an EBM3.4 specimen (after HIP) is illustrated in Fig. 6 (all batches showed the same microstructure except for the porosity), where these corrugated boundaries and the limits of the melt pools can be seen. In addition, the presence of ultra-fine precipitates can be inferred in Fig. 6b, thanks to the voids they leave (dark dots) upon removal from the Cu matrix due to the chemical etching. Elongated particles of Zr<sub>2</sub>O<sub>3</sub> (previously identified in earlier batches [31]) were also detected (Fig. 7, EBM3.4 after HIP), oriented perpendicular to the building direction and frequently associated to irregular pores and lack of fusion defects. EDS analyses revealed high Zr (~80 wt.%) and O (~20 wt.%) concentrations (Fig. 8) in these particles.

Fig. 9a, an FE-SEM micrograph of an EBM3.4 specimen (after HIP), shows sub-micron precipitates ( $\leq 300$  nm) often found at the boundaries of the melt pools. These precipitates exhibited a higher concentration of Zr with minor amounts of Cr, as supported by the EDS analyses shown in Figs. 9b and 10. FE-SEM and TEM characterization were performed to confirm the presence of precipitates smaller than 100 nm, previously reported by other authors in conventionally manufactured CuCrZr [39, 40]. Fig. 11 depicts FE-SEM micrographs obtained from an EBM3.4 specimen in the as-built state and after HIP. A homogeneous distribution of fine precipitates ( $\leq 100$  nm; dark dots in the micrograph) can be observed in both conditions.

Two methods were used to obtain suitable specimens for TEM analyses: the carbon extraction replica technique and conventional thin foil preparation. Initially, it was anticipated that the former would provide a comprehensive characterization of these precipitates, but encountered challenges in extracting from the Cu matrix the finest precipitates ( $\leq 10$  nm). Fig. 12 displays a TEM micrograph along with its EDS analyses from a carbon replica of an EBM3.4 specimen (after HIP), revealing the presence of Cr-rich precipitates with sizes up to 100 nm. Furthermore, in Fig. 13a, a thin foil obtained from an EBM3.4 specimen (after HIP) reveals a uniform distribution of extremely fine precipitates, some even smaller than 10 nm (bright dots), as illustrated in Fig. 13b and 13c. EDS linescan analyses over these ultra-fine precipitates reaffirmed their Cr-rich nature (Fig. 14).

One last microstructural feature can be deduced from the micrographs presented. Upon closer examination of Figs. 6b or 9a, one might consider that the fine Cr-rich precipitates are aligned following different directions. These orientations are directly related to a solidification-enabled cellular-like microstructure compound of very fine columnar subgrains developed during the EB-PBF process. Subgrain structures of EBM3.4 (after HIP) can be observed in Fig. 15a. The different orientations of these substructures are easily visible in this micrograph: the red box indicates a region where these columnar subgrains are clearly seen. Conversely, in the region highlighted by the black box in Fig. 15b, these elongated subgrains are pointing directly towards the observer, revealing the cellular-like structure perfectly.

### 3.4. Mechanical characterization

The engineering stress-strain curves obtained from EBM3.4 specimens are shown in Fig. 16a. Due to the high porosity found in EBM-TLS specimens (also after HIP), obtaining reliable tensile results proved challenging, leading to significant scatter. One engineering stress-strain curve obtained at RT from an EBM-TLS specimen has also been included in Fig. 16a to facilitate comparison between the EBM-TLS and EBM3.4 batches. Two EBM3.4 specimens were tested at RT, two at 250 °C and one at 350 °C. Conversely, EBM-TLS (a total of nine small tensile specimens) was only tested at RT. This limited number of specimens reflects the current screening phase of our research, where several fabrication process EB-PBF parameters are being tested to produce materials with high relative density values and superior mechanical properties. Table 5 summarizes the tensile properties obtained from EBM3.4 and EBM-TLS, for comparative purposes. The behaviour of both batches in the elastic regime is quite similar, although EBM-TLS exhibited higher yield strength ( $R_p$ ) in almost all specimens. In the plastic regime, the Ultimate Tensile Strength (UTS) obtained from EBM-TLS showed high scattering with values ranging from 415 to 455 MPa (at RT). In the case of EBM3.4, 449 MPa, 329 MPa and 304 MPa were obtained from testing at RT, 250 °C and 350 °C, respectively. The major discrepancy between both fabrications, in terms of mechanical properties, is the elongation capacity, as illustrated by the significant difference between the uniform elongation (UE) achieved by EBM-TLS (7.8 %) and that obtained from EBM3.4 (17 %), both at RT. For the rest of the tensile-tested specimens in EBM-TLS, the values for UE (at RT) ranged between 6 % and 10 %. Total elongation (TE) values recorded for EBM-TLS (at RT) ranged between 7 % and 11.5 %, while EBM3.4 showed 29 %, 19 % and 14 % at RT, 250 °C and 350 °C, respectively. Fig. 16b illustrates the Charpy impact behaviour of EBM-TLS and EBM3.4 at RT. Four miniaturized Charpy specimens were tested from EBM-TLS, while nine specimens from EBM3.4 were also subjected to Charpy testing. All impact tests were conducted at RT due to

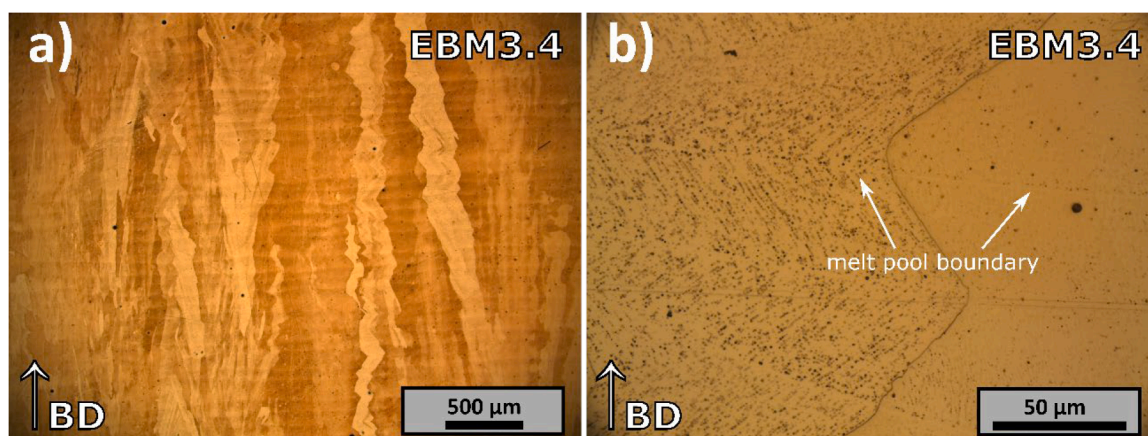


Fig. 6. OM micrographs of EBM3.4 after HIP. The typical elongated zigzag microstructure, melt pool boundaries and the presence of ultra-fine precipitates (dark dots resulting from precipitates leaving the Cu matrix after chemical etching) are shown (BD: Building Direction).

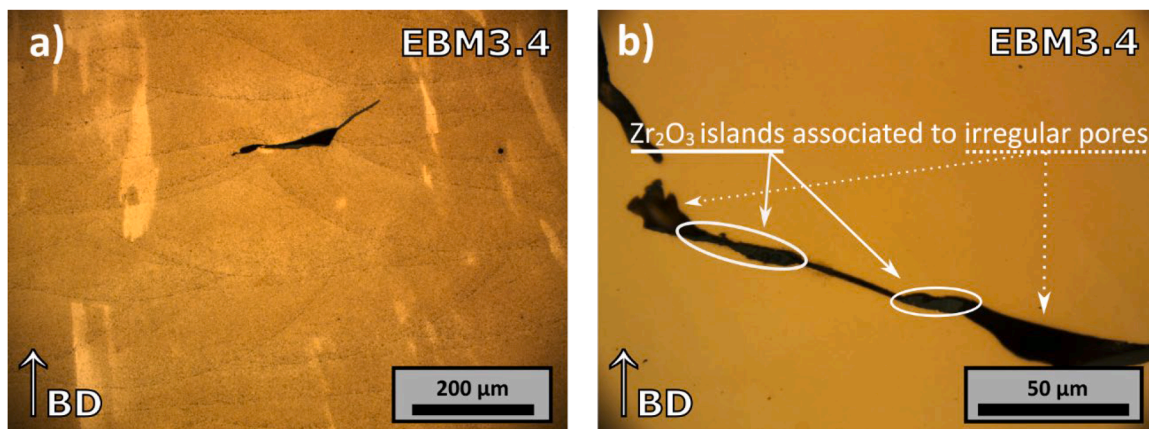


Fig. 7. OM micrographs of EBM3.4 after HIP. Zr<sub>2</sub>O<sub>3</sub> elongated particles predominantly oriented perpendicular to the Building Direction (BD), and often related to lack of fusion and porosity defects.

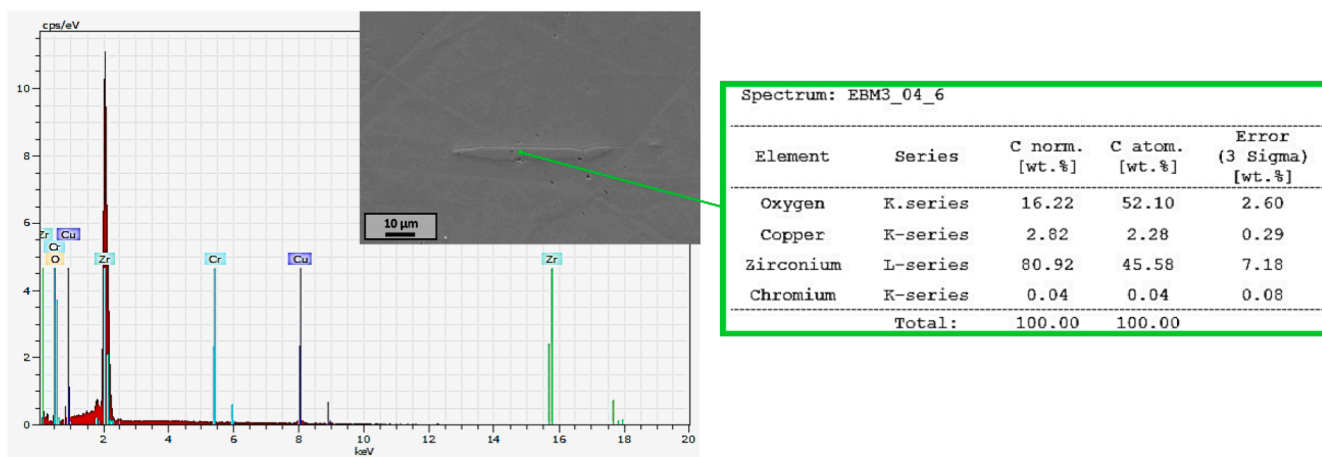


Fig. 8. EDS analyses conducted on Zr<sub>2</sub>O<sub>3</sub> particles, frequently found perpendicular to the Building Direction (BD).

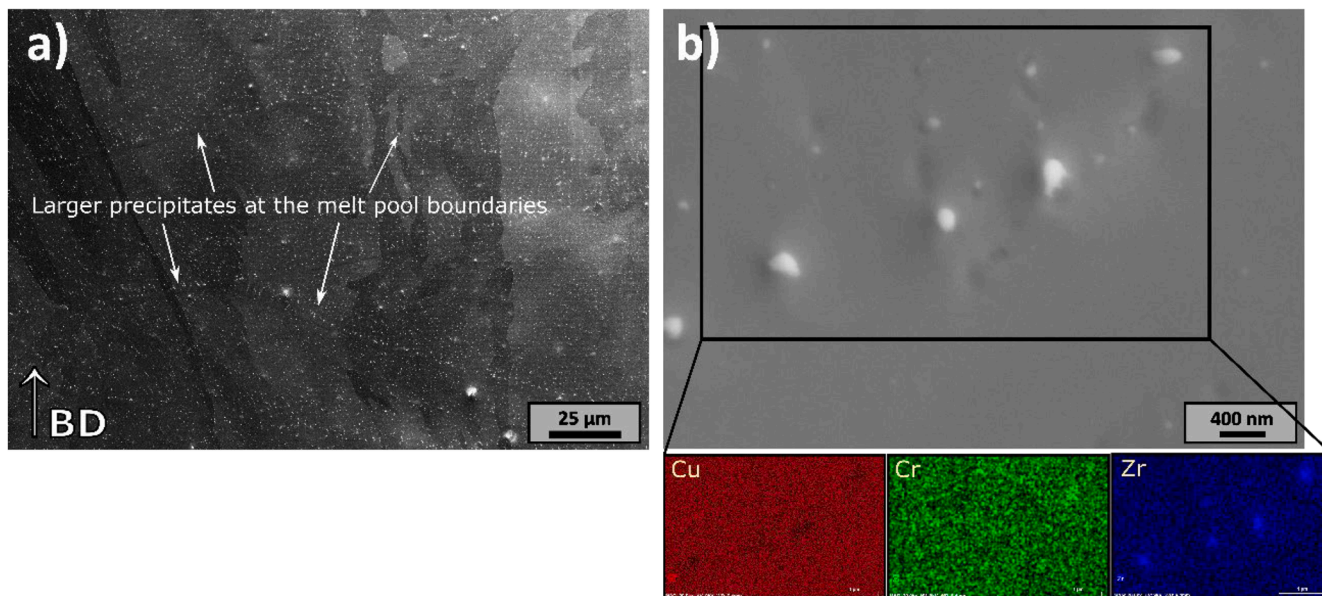


Fig. 9. FE-SEM micrographs of EBM3.4 after HIP. (a) Zr-rich precipitates detected mainly at the melt pool boundaries (FE-SEM micrograph obtained with the InLens detector); (b) EDS analysis showing the Zr-rich nature of these precipitates.

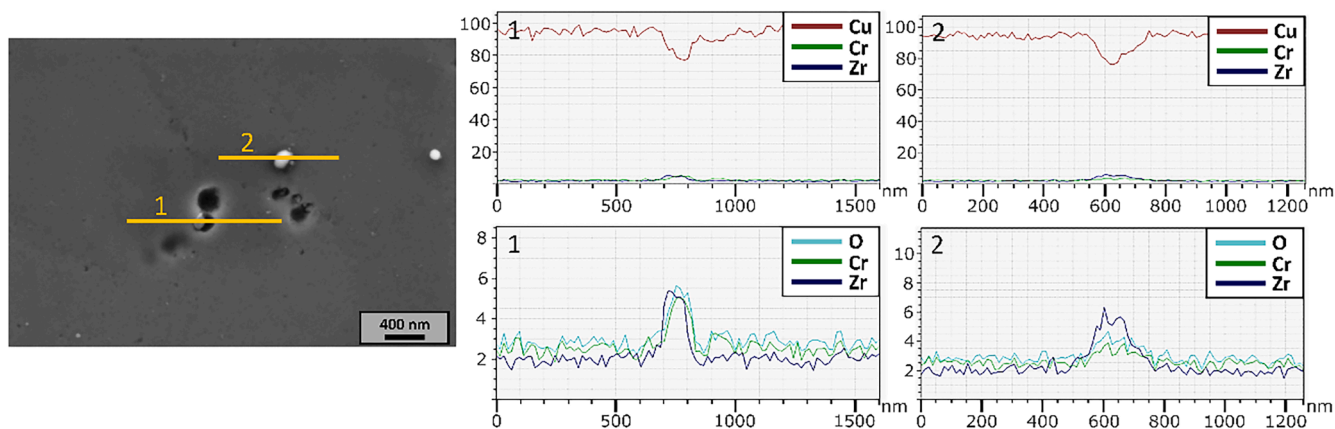


Fig. 10. FE-SEM micrograph of EBM3.4 after HIP and EDS linescans showing some amounts of Cr in Zr-rich precipitates.

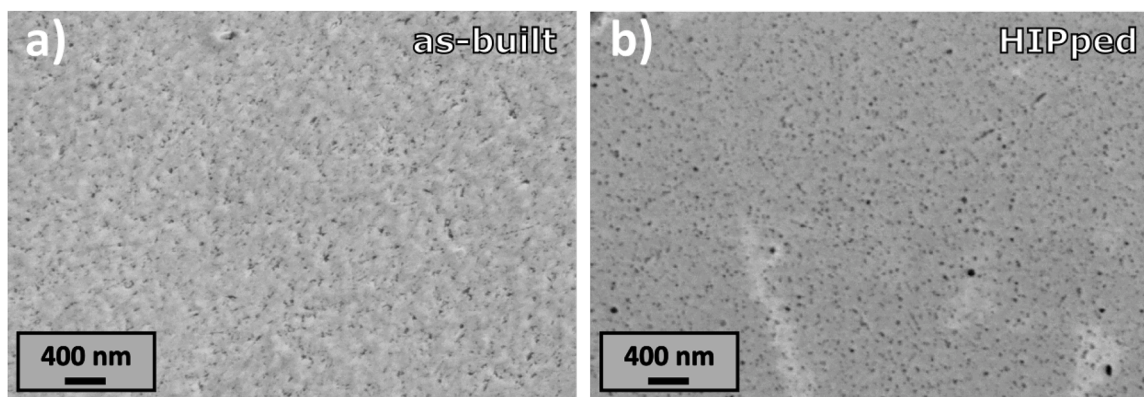


Fig. 11. FE-SEM micrographs of EBM3.4 in the (a) as-built condition and (b) after HIP.

limitations in material availability associated with the screening phase or laboratory-scale nature of this research; however, future batches will be also tested at the operational temperature range of this alloy (250 °C / 350 °C) [7]. Among the EBM3.4 specimens, three were machined from each of the bars designated as EBM3.4\_C1, EBM3.4\_C2 and EBM3.4\_C3, respectively (see Fig. 2b). Once more, the higher porosity observed in EBM-TLS resulted in inferior performance compared to EBM3.4, with values of  $34.5 \pm 3.0$  J/cm<sup>2</sup> and  $48.6 \pm 1.7$  J/cm<sup>2</sup>, respectively.

Analyses of the fracture surfaces of tensile specimens shows the typical features of a highly ductile fracture (Fig. 17), but significant differences can be observed comparing both EBM batches. Lack of fusion defects with embedded particles were detected in all EBM-TLS specimens (Fig. 17a), consistent with the poor tensile results obtained in this batch in terms of deformation capacity. In addition, the fractographic analysis revealed an interesting feature displayed in Fig. 18: a hard and brittle Zr<sub>2</sub>O<sub>3</sub> particle which could have acted as a stress concentrator, thereby decreasing the mechanical strength. The average hardness values obtained from all the materials fabricated were significantly higher than the ITER recommended values (126 HV [41]). Even in the as-built condition, the average hardness values reached  $143 \pm 9$  HV0.5, while for the tensile tested batches (after HIP), the values were  $149 \pm 8$  HV0.5 for EBM3.4 and  $174 \pm 4$  HV0.5 for EBM-TLS.

## 4. Discussions

### 4.1. Gas atomization

As mentioned earlier, gas-atomized CuCrZr-3 powder has demonstrated notable advancements in powder manufacturing techniques, building on the knowledge gained from our prior investigation [31]. In

contrast, the high density of agglomerates and satellites shown by CuCrZr-TLS may detrimentally affect the flowability and spreadability of the powder during printing. The improvement in the quality of CuCrZr-3 batch is attributed to an enhanced control of powder temperature during atomization, precise management of powder quantity in the hopper, and mitigation of overheating that could foster agglomerate and satellite formation. Regarding the chemical composition of each batch, it should be emphasized the low levels of oxygen and aluminium achieved (Table 1). While it is vital to keep the aluminium content as low as possible to avoid activation issues [42], minimization of the oxygen concentration is also essential in order to avoid the creation of zirconium oxides during the EB-PBF fabrication process. Based on the acquired knowledge, precise control of the atmosphere during the EB-PBF manufacturing is imperative to minimize the oxygen concentration.

### 4.2. Relative density and thermal conductivity

The  $\rho_{rel}$  results obtained from the different EB-PBF batches fabricated are highly indicative of which EB-PBF fabrication process parameters appears to have the most influence on the quantity and morphology of pores produced. The nature of porosity observed in EBM-TLS, EBM3.2 and EBM3.3 batches directly correlates with the low energy absorbed by the metal powder bed during EB-PBF manufacturing. Conversely, for the EBM3.1 batch, the combination of fabrication parameters provided an increase of the energy absorbed by the powders, resulting in a homogeneous distribution of spherical and individual pores. HIP treatment is expected to remove the eventual residual porosity; nevertheless, its efficacy hinges on the porosity's characteristics: spherical and isolated pores are more susceptible to elimination, while irregularly-shaped and interconnected pores may pose challenges or even resist removal during

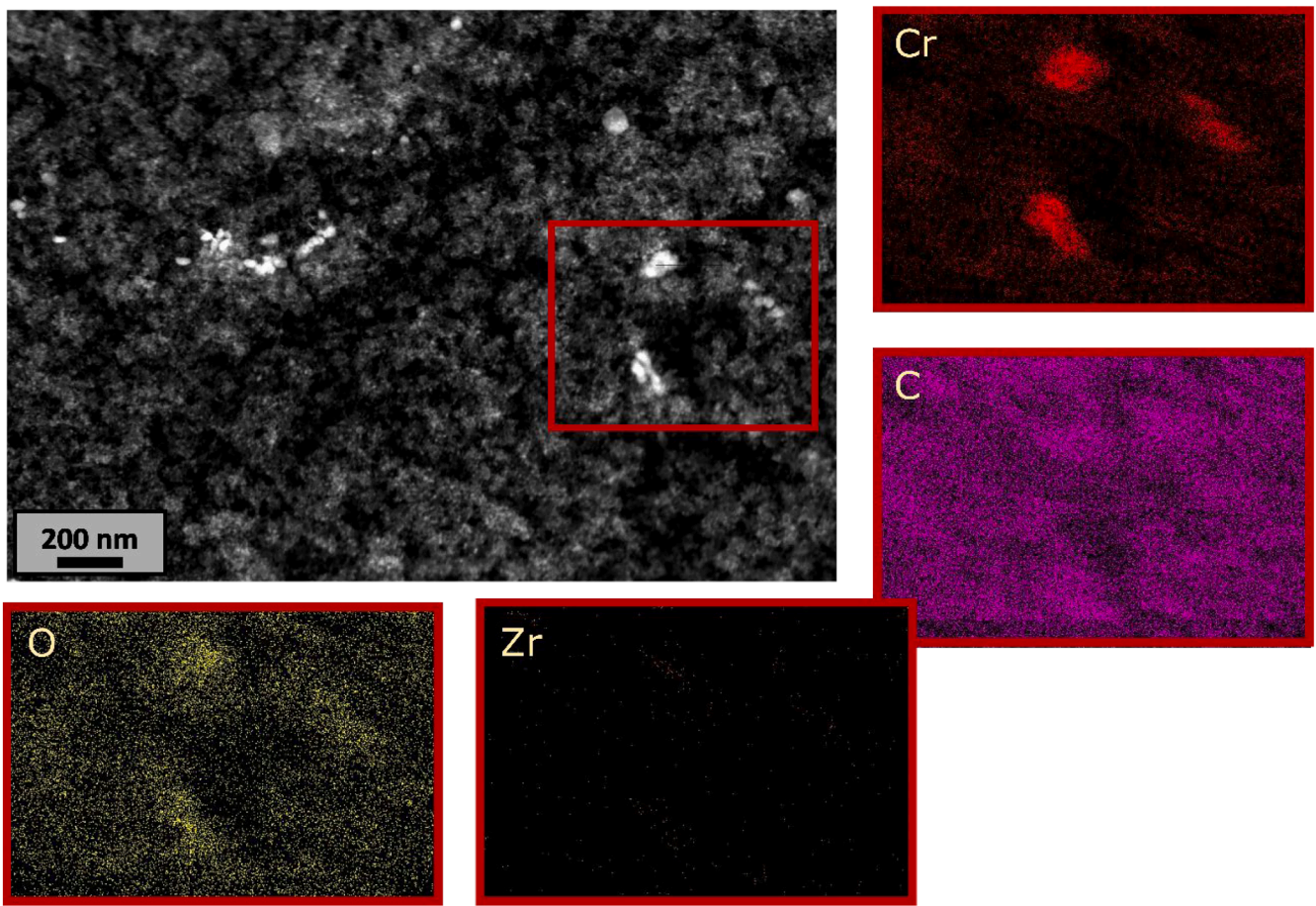


Fig. 12. TEM micrograph along with its EDS analyses from a carbon replica of an EBM3.4 specimen (after HIP).

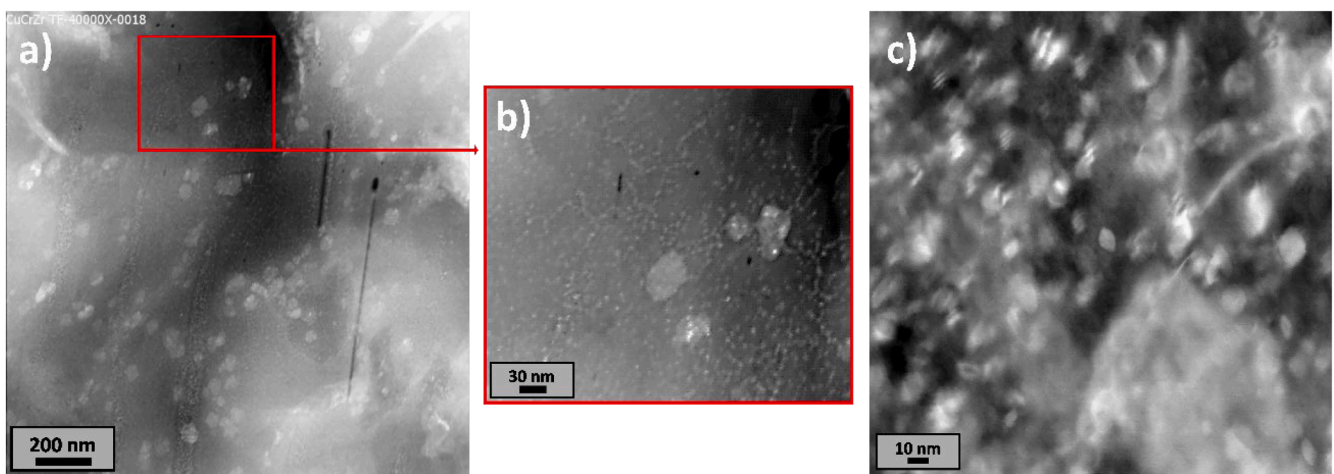


Fig. 13. TEM micrographs from a thin foil extracted from an EBM3.4 specimen (after HIP). The Cr-rich precipitates of smaller size are detectable as bright spots in (a) and (b), while they are fully visible in (c) due to the higher magnification.

HIP treatment. Additionally, the size of the pores requires an important consideration, as larger pores are less likely to be effectively removed by HIP treatment. To leverage the benefits of the post-build HIP treatment, the fabrication process parameters for EBM3.4 were adjusted to significantly increase the energy absorbed by the powders during manufacturing, thereby minimizing the presence of irregular and interconnected pores. As anticipated, after the addition of the HIP treatment, only EBM3.1 and EBM3.4 obtained an increase in their  $\rho_{rel}$

values (porosity values  $<0.5\%$ ). Porosity represents discontinuities within the microstructure that degrade thermal conductivity. This is particularly relevant in High Heat Flux (HHF) components where optimum thermal conductivity is essential to ensure effective performance. The thermal conductivity results obtained from EBM3.4 (ranging from 345 to 360 W/m•K) are in the same direction of the desired thermal performance criteria outlined for ITER, as indicated in Table 1 under the ITER requirements column.

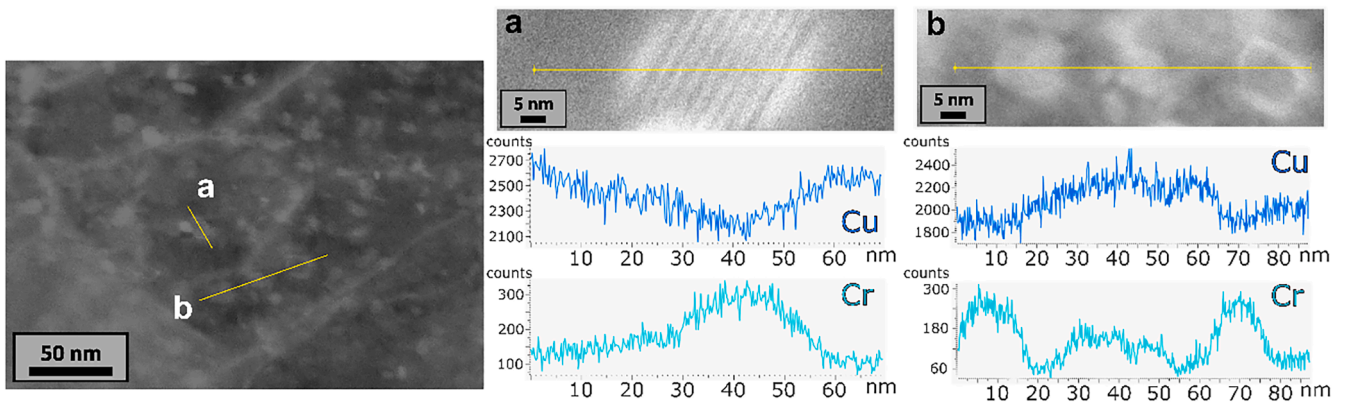


Fig. 14. EDS linescan analyses (performed on TEM) of ultra-fine precipitates showing their Cr-rich nature.

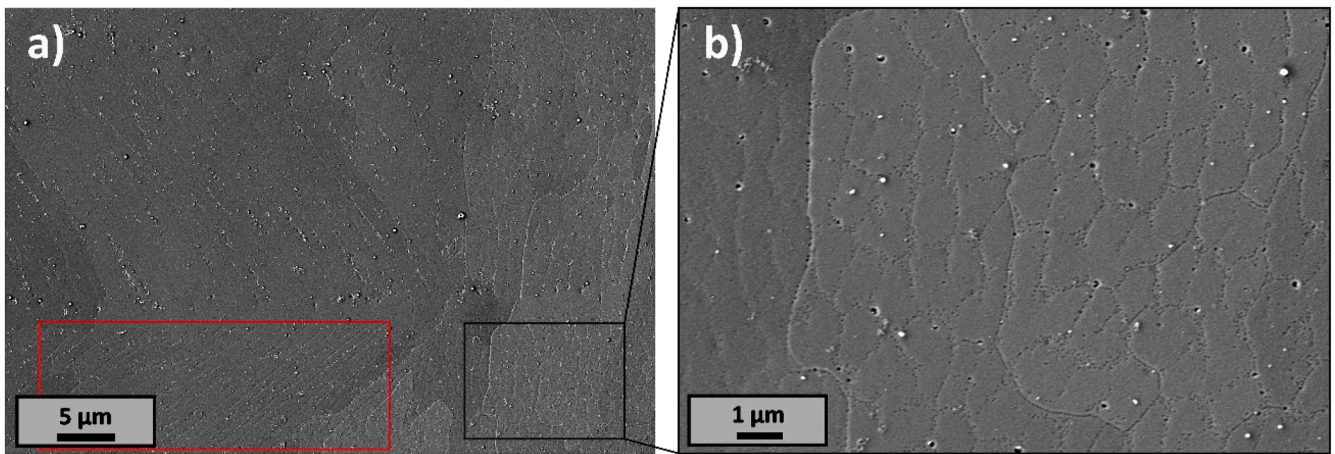


Fig. 15. FE-SEM micrographs of EBM3.4 after HIP. Solidification-enabled cellular-like subgrains can be observed with varying orientations. The red box region highlights subgrains oriented upwards, while the black box zone region (zoomed in (b)) showcases subgrains pointing towards the observer, clearly displaying the cellular-like structure. (For interpretation of the references to colour in this figure legend, the reader is referred to the web version of this article.)

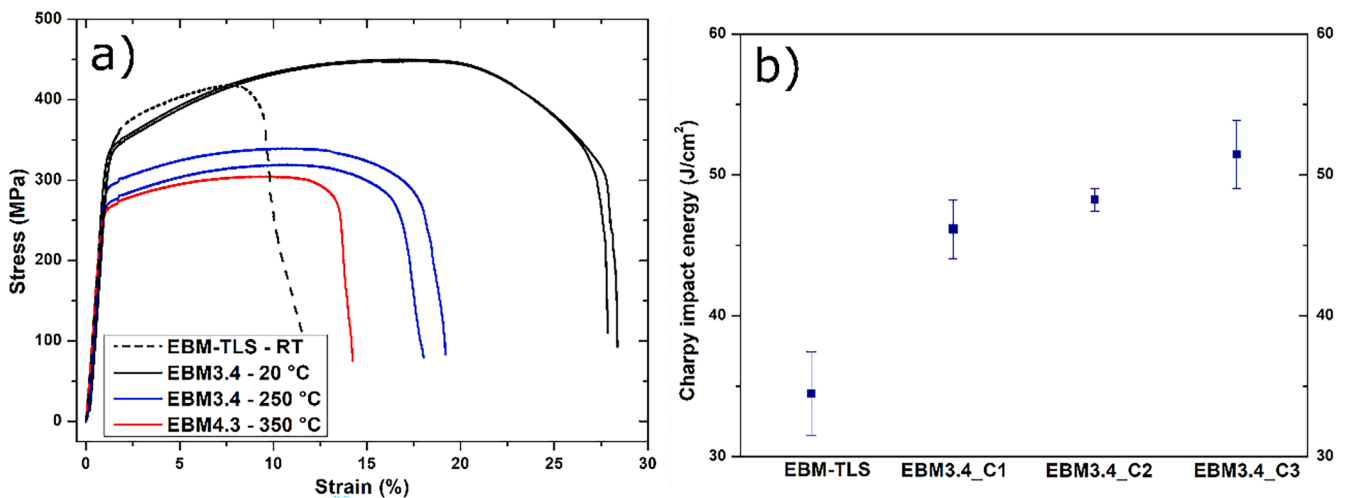


Fig. 16. (a) Engineering stress-strain curves obtained from EBM3.4 specimens. Additionally, a curve from the tensile testing of EBM-TLS specimens has been included for comparison, highlighting the outstanding performance of EBM3.4; (b) Charpy impact behaviour of EBM-TLS and EBM3.4 after HIP.

4.3. Microstructural analysis before and after HIP treatment

Fig. 6a shows the typical elongated and zigzag grain structure, parallel to the building direction, of PBF-manufactured materials [24,25,

27,30,31,36–38]. Such structure typically arises as a result of the 90° rotation of the scan pattern during the AM process, which in turn induces a similar rotation of the thermal gradients in the melt pools [43, 44]. Optical and electron microscopy revealed the existence of different

**Table 5**

Tensile properties obtained from EBM3.4 (after HIP, tested at RT, 250 °C and 350 °C) and EBM-TLS (after HIP, tested at RT). The average values for SAA CuCrZr, sourced from the SDC-IC [16], are also included for comparison. Additionally, Young's modulus measurements obtained using the Impulse Excitation Technique and the hardness values are provided.

	EBM-TLS	EBM3.4			SAA CuCrZr (average values, [16])		
		20 °C	250 °C	350 °C	20 °C	250 °C	350 °C
UTS (MPa)	415–455	449	329	304	405	315	274
Rp (MPa)	345–384	333	273	258	287	244	217
UE (%)	6–10	17	11	9	18.4	13.7	13.2
TE (%)	7–11.5	28	19	14	27.0	21.0	23.0
E <sup>i</sup> (GPa)	–	123.5	–	–	125	117	110
HV0.5 <sup>ii</sup>	174 ± 4	149 ± 8	–	–	126	–	–
λ (W/ (m•K))	–	345–360	–	–	318	345	347

i. Young's modulus values for SAA CuCrZr are referenced to the ITER Material Properties Handbook (MPH) of CuCrZr [4]. Young's modulus values obtained from EBM3.4 and EBM-TLS were measured employing the Impulse Excitation Technique, according to recommendations provided in [4].

ii. Hardness value recommendation for CuCrZr-ITER grade is referenced to [41].

types of precipitates in the microstructure. The large and elongated Zr<sub>2</sub>O<sub>3</sub> particles detected (previously identified in earlier batches [31]) adversely affect mechanical properties (Figs. 7, 8 and 18). While Zr contributes to grain refinement and enhances the homogeneity of the precipitate distribution, it is inherent in its nature to act as a significant oxygen getter [4,8]. Upon reacting with O to form zirconium oxides, the

potential benefits of Zr diminish, leading to a reduction in final mechanical properties. This fact highlights the importance of not only reducing the oxygen concentration in the atomization atmosphere during future gas atomization processes, but also paying special care when handling atomized powders to prevent their superficial oxidation during storage prior to additive manufacturing. Adequate solutions, like vacuum, dehumidification or storage under protective atmosphere are convenient for Cu alloys.

The presence of a homogeneous distribution of fine precipitates, smaller than 100 nm, was confirmed in the as-built state and after HIP (Fig. 11; dark dots in the micrograph). A comparison of the microstructure before and after HIP treatment suggests a slight increase in the density of precipitates and a very slight coarsening of precipitates after HIP. This statement is supported by the increase in hardness after the HIP process (see Section 3.4). However, this modest increment falls within the range of experimental error, therefore further confirmation through a detailed TEM study is required to confirm this. EDS analyses performed in TEM unveiled the Cr-rich nature of these precipitates (Figs. 12 and 14). Additionally, TEM analysis confirmed the presence of a uniform distribution of very fine Cr-rich precipitates (<10 nm), as shown in Fig. 13. This distribution is highly beneficial for the mechanical properties of a precipitation-hardened alloy like CuCrZr.

At this point, it is important to consider the Cr content of the EBM3 batches (0.95 wt.%), which slightly exceeds the maximum allowed for the ITER Grade of CuCrZr (0.90 wt.%, [5]). This upper limit originates from the conventional manufacturing of CuCrZr through traditional methods (casting or forging), where the cooling rates after subjecting the material to heat treatments at high temperatures may not be fast enough to prevent coarsening of the precipitates. As a result, a limitation of the Cr content became necessary to avoid the formation of excessively

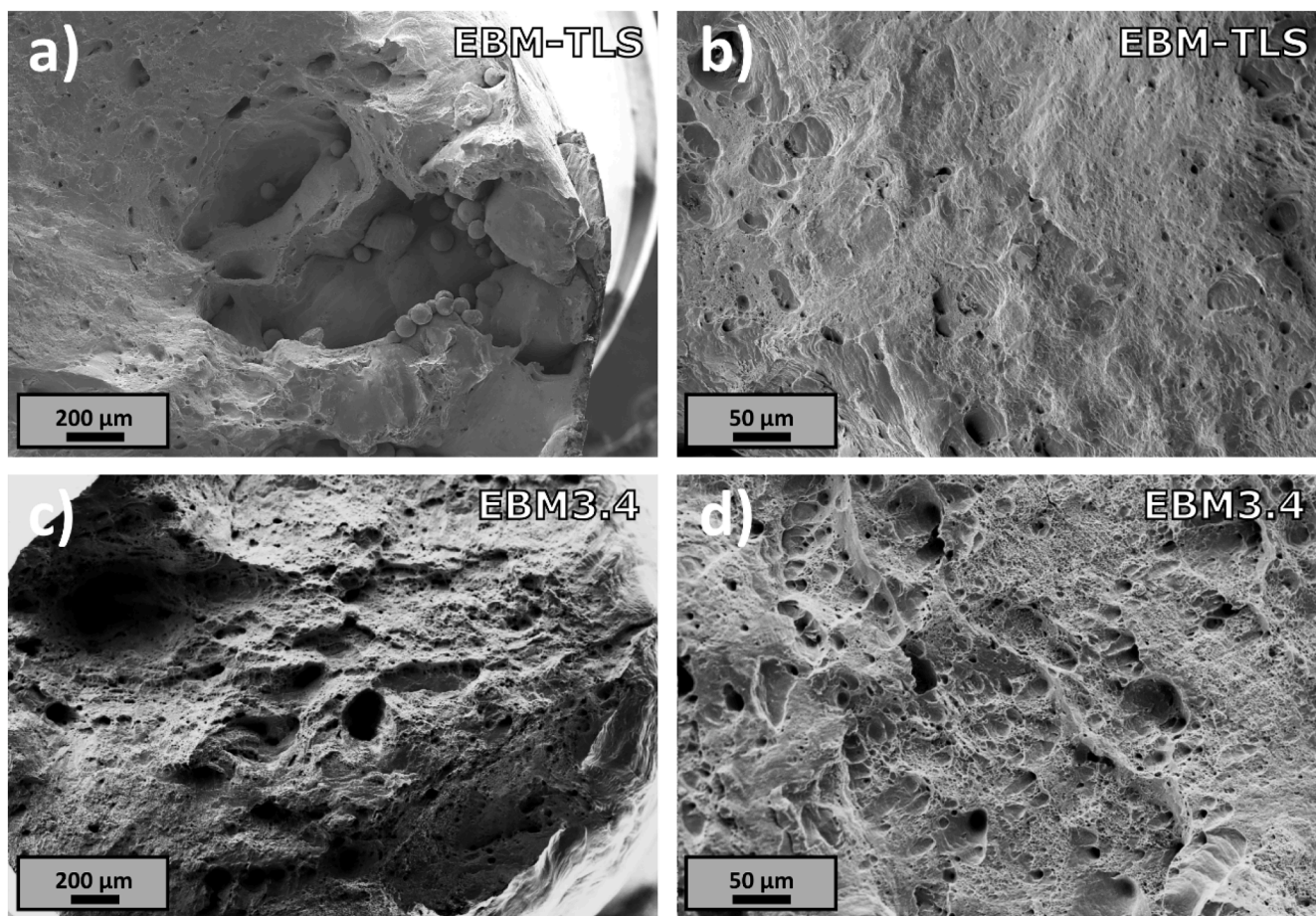


Fig. 17. FE-SEM micrographs of fracture surfaces from tensile testing specimens: (a) and (b) EBM-TLS, and (c) and (d) EBM3.4.

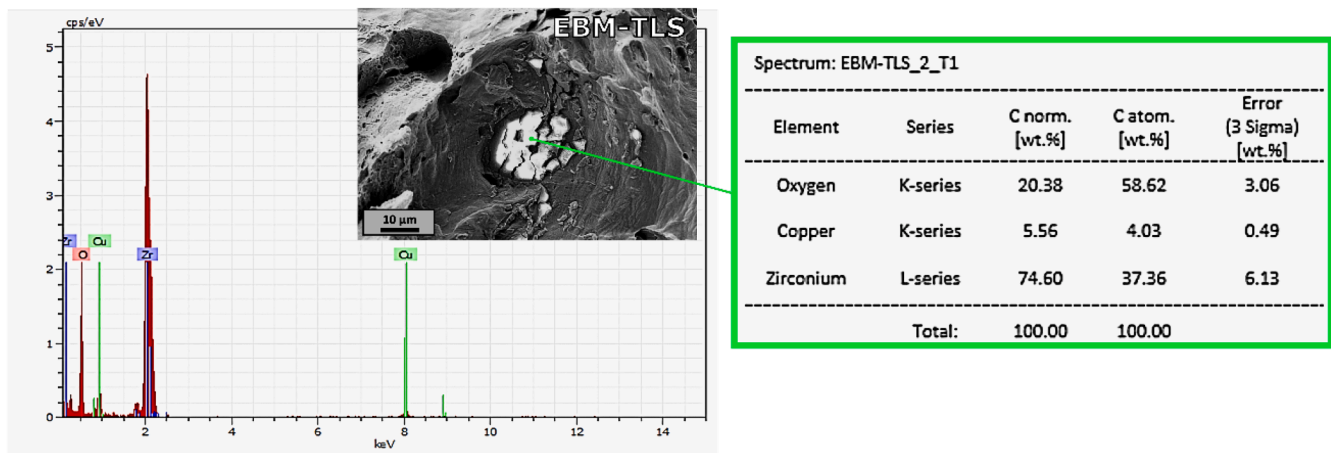


Fig. 18. FE-SEM micrograph of the fracture surface from an EBM-TLS tensile testing specimen with its EDS analysis. Zr<sub>2</sub>O<sub>3</sub> island can be observed, possibly associated with a pore, which could act as a stress concentrator.

coarse precipitates, which can significantly influence the deformation mechanisms activated when stress is applied, thereby affecting the mechanical properties of the alloy. In precipitation-hardened alloys, it is widely recognized that precipitate sizes should be approximately less than 100 nm. Beyond this threshold, their ability to pin dislocations becomes ineffective and their contribution to mechanical strength is reduced [6]. As mentioned above, PBF additive manufacturing technologies involve rapid melting and solidification of the metal powder bed, which may lead to the formation of an ultra-fine state of precipitates already in the as-built condition. Our findings, based on the fabrication of CuCrZr using EB-PBF, demonstrate the presence of an ultra-fine state of precipitates directly in the as-built condition. We suggest that this microstructure is attributed not only to the rapid melting and solidification of the metal powder bed involved in the EB-PBF process, but also to the high temperatures achieved within the powder bed during printing, which act as an ageing heat treatment. This indicates that exceeding the upper limit specified for Cr in the ITER Grade of CuCrZr does not pose a risk of precipitate coarsening in components obtained by PBF technologies.

Finally, it is important to emphasize the intricate microstructure achieved through the EB-PBF method, which exhibits a hierarchical nature characterized by multiple scale lengths: conventional grains and grain boundaries, typically spanning several tens of μm, which coexist with solidification-enabled cellular-like subgrains, which are generally smaller than 1 μm. Furthermore, ultra-fine precipitates contribute to further complexity and refinement within this hierarchical architecture. With regard to the subgrains, similar substructures have been previously reported in other materials fabricated using L-PBF [45–49]. Their origin was attributed again to the rapid and repeated thermal cycles (melting and solidification during L-PBF or EB-PBF), where the high cooling rates and the strong thermal gradients developed in the process result in a limited solid redistribution and chemical segregation at a nanometric scale [45,49].

#### 4.4. Mechanical properties

The substantial differences obtained in the tensile testing results between EBM-TLS and EBM3.4 can primarily be attributed to the higher  $\rho_{rel}$  values achieved in EBM3.4. The elongation capacity is strongly affected by porosity, as it leads to a reduction in the effective cross-sectional area of the tensile specimens. Moreover, the analysis of the fracture surfaces reveals the correlation between large and irregular pores, frequently interconnected, with lack of fusion defects (Fig. 17a), and the presence of considerable Zr<sub>2</sub>O<sub>3</sub> precipitates that could compromise the mechanical properties of the material. The high

porosity and population of defects in EBM-TLS are explained mainly by two reasons: Firstly, the high scanning speed used to fabricate EBM-TLS impedes the correct absorption of energy necessary for powder melting during the EB-PBF process. Secondly, the higher oxygen content found in CuCrZr-TLS powders contrasts with the low values obtained when atomizing our own powders. This difference may be due to suboptimal gas atomization combined with inadequate handling of the manufactured powders, which may lead to their oxidation. Once again, it is essential to emphasize the critical role of minimizing oxygen content in PBF fabrications, particularly for Cu-alloy applications.

Figs. 19–21 summarize the tensile properties reported by other authors for CuCrZr-ITER Grade. Average and minimum curves for conventional CuCrZr in the SAA (Solution Annealed and Ageing) and in the SCA (SAA + HIP treatment) conditions are presented (adapted from

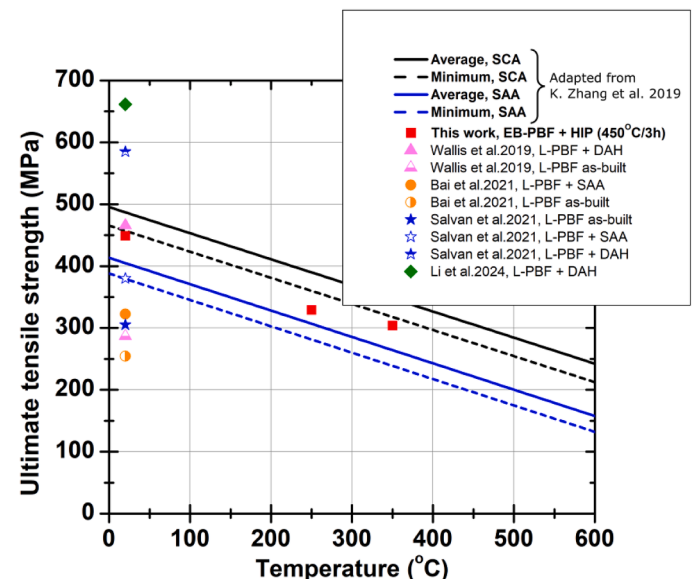


Fig. 19. Minimum and average Ultimate Tensile Strength (UTS) curves for Solution Annealed and Aged (SAA) CuCrZr (in blue) and for Solution Annealed and Aged + HIPped (SCA) CuCrZr (in black), gathered and developed by K. Zhang et al. [4]. The UTS values obtained in this work (red squares) from EB-PBF-manufactured CuCrZr are provided. Additionally, UTS values obtained from L-PBF-manufactured CuCrZr, previously published by other authors are included for comparison [23,24,38,52]. (For interpretation of the references to colour in this figure legend, the reader is referred to the web version of this article.)

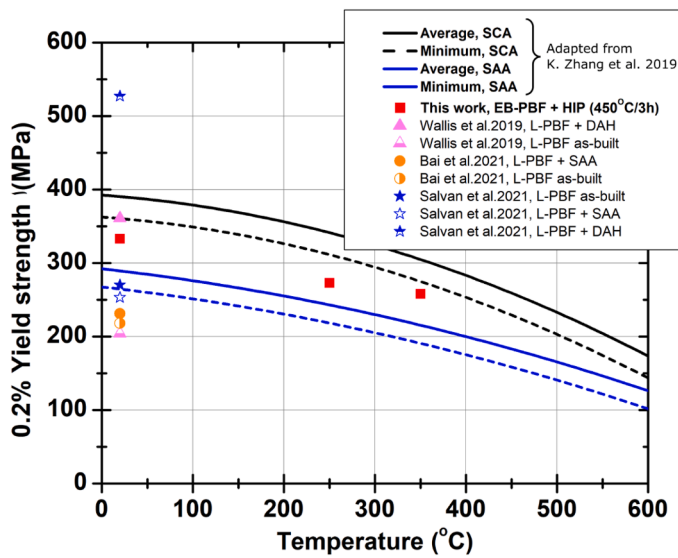


Fig. 20. . Minimum and average 0.2 % Yield Strength (Rp) curves for Solution Annealed and Aged (SAA) CuCrZr (in blue) and for Solution Annealed and Aged + HIPped (SCA) CuCrZr (in black), gathered and developed by Zhang et al. [4]. The Rp values obtained in this work (red squares) from EB-PBF-manufactured CuCrZr are provided. Additionally, Rp values obtained from L-PBF-manufactured CuCrZr, previously published by other authors are included for comparison [23,24,38]. (For interpretation of the references to colour in this figure legend, the reader is referred to the web version of this article.)

Ref. [4]). Fig. 21 includes data from the works carried out in Refs. [10, 50,51]. In addition, reported tensile properties for CuCrZr manufactured by L-PBF are included [23,24,38,52]. The Young’s modulus has been only measured at RT, obtaining a value of 123.5 GPa, which aligns with the average value of 125 GPa reported for solid CuCrZr in the SAA state [4]. In terms of UTS and Rp, EB-PBF results obtained in this work are promising, comparable or even better than those obtained with SAA CuCrZr. Furthermore, present results are remarkable when compared to those obtained with L-PBF – CuCrZr. While microstructures obtained using L-PBF are similar to those achieved through EB-PBF, subtle differences lead to significant variations in mechanical properties. Reported works by Salvan et al. [24] and Li et al. [52] agree in achieving

high UTS and YS values after application of Direct Age Hardening (DAH) to L-PBF as-built specimens, which they mainly attributed to a combined effect of precipitation strengthening and high dislocation density associated with solidification-enabled cellular-like subgrain boundaries. Notably, no Cr-rich nanoprecipitates were detected in the as-built condition of their L-PBF-manufactured specimens, highlighting the necessity of DAH treatment to achieve the proper microstructure and excellent mechanical properties.

Conversely, EB-PBF-manufactured specimens in this study exhibit a homogeneous distribution of Cr-rich nanoprecipitates already in the as-built condition, with only minimal coarsening and density increase of precipitates observed after the HIP treatment under SEM microscopy (confirmation by in-depth TEM analysis is required to confirm this statement). This suggests the superior efficiency of the electron-based technology over laser-based methods, as the use of an electron beam leads to more efficient energy absorption during the process, which seems to favour the formation of nanoprecipitates more easily during the rapid melting and subsequent cooling process with high cooling rates than in the L-PBF process. Microstructures of L-PBF fabricated materials after DAH and our EB-PBF produced material after HIP appear very similar, with a homogeneous dispersion of Cr-rich nanoprecipitates and a high dislocation density associated with subgrain boundaries. This combination of a homogeneous dispersion of nanometric Cr-rich precipitates and a high dislocation density likely contributes significantly to the exceptional mechanical performance observed in our study. However, the superior mechanical performance observed in Salvan et al. [24] and Li et al. [52] suggests that the dispersion of precipitates in these L-PBF specimens might be even more refined. Moreover, recent laser-based studies [53,54] have not achieved the exceptional condition of Cr-rich nanoprecipitates demonstrated here, resulting in reduced mechanical performance compared to the tensile properties obtained in our study.

When considering the elongation capacity, it is essential to compare our results (highlighted with red squares in Fig. 21) with those of solid CuCrZr, denoted by symbols in green, purple, and cyan from studies by Li et al. (2009) [10], Fabritsiev et al. (1998) [50], and Tähtinen et al. (1998) [51], respectively, as shown in Fig. 21. With the exception of the high total elongation obtained at elevated temperatures in Ref. [50], our results are alienated to those observed for solid CuCrZr under both SAA and SCA treatments. These findings are highly promising as they point towards further enhancements. Our aim is to achieve relative densities even higher than the 99.5 % achieved in EBM3.4. Additionally, reducing

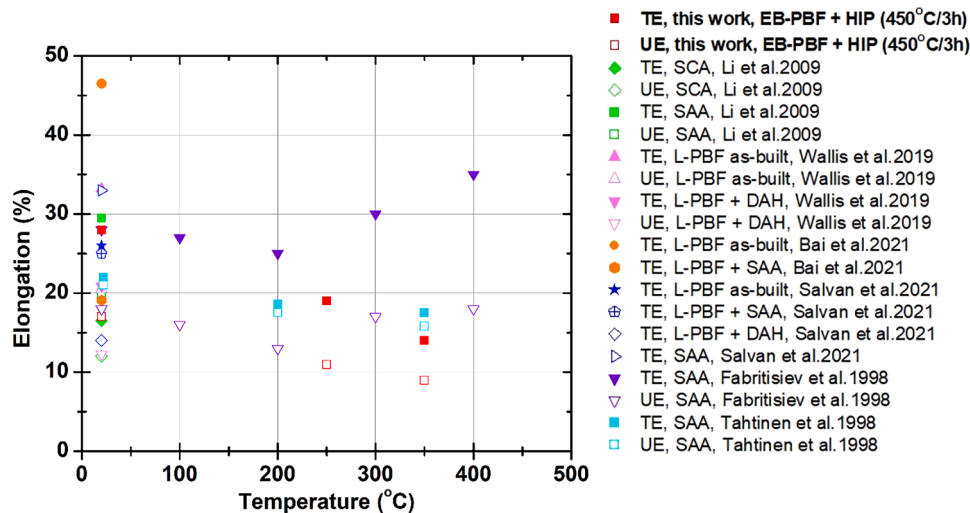


Fig. 21. Total Elongation (TE) and Uniform Elongation (UE) values obtained in this work (red squares) from EB-PBF-manufactured CuCrZr. Additionally, the previously reported values from Solution Annealed and Aged (SAA) CuCrZr [24,50,51], Solution Annealed and Aged + HIPped (SCA) CuCrZr [10] and L-PBF-manufactured CuCrZr [23,24,38] are included. (For interpretation of the references to colour in this figure legend, the reader is referred to the web version of this article.)

the oxygen content remains a focus for future improvements, with the goal of further diminishing the presence of  $Zr_2O_3$  islands in the microstructure. With regard to the Charpy impact behavior, EBM3.4 showed promising results at RT; however, there is room for improvement in this aspect. Previous studies on solid SAA CuCrZr [55] have reported slightly better performance ( $75 \text{ J/cm}^2$  compared to our approximate  $49 \text{ J/cm}^2$ ). We anticipate achieving this improvement through further optimization of the EB-PBF fabrication process parameters, aiming to approach closer to 100 %  $\rho_{rel}$ .

In terms of the hardness obtained, it is indeed noteworthy that all the EB-PBF batches fabricated, irrespective of the  $\rho_{rel}$  value, exhibited hardness values exceeding the specification for CuCrZr-ITER Grade (126 HV [41]). Fig. 22 shows the average hardness values of all the EB-PBF batches presented in this study together with the average values obtained from previously reported batches [31]. In addition, this graph sheds some light on the role of the alloying elements (Cr and Zr) on hardness. Interestingly, despite the irregular and large porosity found in EBM-TLS, its hardness considerably exceeds that obtained from EBM3.4, a fact that is consistent with the higher yield strength achieved by EBM-TLS. This can be easily explained by the higher Zr content in EBM-TLS (0.12 wt.%) compared to EBM3.4 (0.063 wt.%), as evidenced in Fig. 22. The graph clearly illustrates the significant influence of Zr on the final hardness, whereas the influence of Cr seems to be relatively lower. An in-depth study of TEM micrographs could corroborate this fact, presumably by detecting the precipitation of CuZr particles at grain boundaries. The coloured boxes in Fig. 22 show the compositional ranges allowed for Cr (in blue) and Zr (in orange) of the CuCrZr-ITER Grade (0.6–0.9 wt.% Cr – 0.07–0.15 wt.% Zr) [4,5]. Despite the wider compositional range allowed for Cr compared to Zr, which might suggest that this element could offer more flexibility in enhancing mechanical properties, it is Zr, with its narrow range that leads to greater increases in the final hardness obtained. However, it is worth remembering that the EB-PBF process offers the flexibility to alloy the material with a relatively high Cr content, potentially exceeding the upper limit slightly. This statement is supported by the homogeneous distribution of nanometric Cr-rich precipitates observed even after HIP (see Section 3.3). In conclusion, high Cr and Zr contents will be used in future EB-PBF fabrications, to take full advantage of additional hardening effects provided by the EB-PBF technique.

To summarize, different microstructural contributions to the final

mechanical properties can be taken into account. The complex microstructure achieved through the EB-PBF method features a hierarchical architecture with multiple scale lengths. This includes conventional grains and grain boundaries, usually spanning several tens of micrometers, alongside smaller, solidification-induced cellular-like subgrains that are generally less than  $1 \mu\text{m}$  in size. Additionally, ultra-fine precipitates add further complexity and refinement within this structure, enhancing the overall material properties in comparison to conventional methods. Moreover, the presence of a high density of dislocations at subgrain boundaries, as highlighted by Salvan et al. [24] and Li et al. [52], plays a significant role in enhancing the mechanical properties.

Therefore, the combined effect of the hierarchical microstructure and the high dislocation density at subgrain boundaries collectively contribute to the outstanding mechanical properties observed in the EB-PBFed CuCrZr alloy. These features underscore the potential of EB-PBF as a viable method for producing high-performance alloys with optimized mechanical properties.

## 5. Conclusions

Gas-atomized CuCrZr powders within the ITER Grade specifications (0.6–0.9 wt.% Cr - 0.07–0.15 wt.% Zr - Bal. wt.% Cu) were used to produce specimens via Electron Beam Powder Bed Fusion (EB-PBF). While powders produced at Ceit (CuCrZr-3) yielded outstanding results, commercial powders (CuCrZr-TLS) exhibited suboptimal conditions for producing nearly fully densified components via EB-PBF. This was attributed to elevated concentrations of satellites, agglomerates, and oxygen. Moreover, the precise control of the atmosphere during the EB-PBF manufacturing process, coupled with careful handling of manufactured powders, is crucial to prevent oxidation during storage prior to additive manufacturing. Densified CuCrZr-ITER Grade was achieved through optimization and careful selection of EB-PBF process parameters. Conclusions drawn from this optimization suggest that facilitating high-energy absorption rates on the powders during process is essential. We anticipate that the margin for reducing the scanning speed will result in higher energy absorption rates and, consequently, relative densities close to 100 %. In this work, scanning speeds were reduced to values  $<200 \text{ mm/s}$  in order to achieve high-energy absorption rates. Low as-built relative density values of 95 % were obtained, which were subsequently increased to 99.7 % after the addition of a Hot Isostatic Pressing

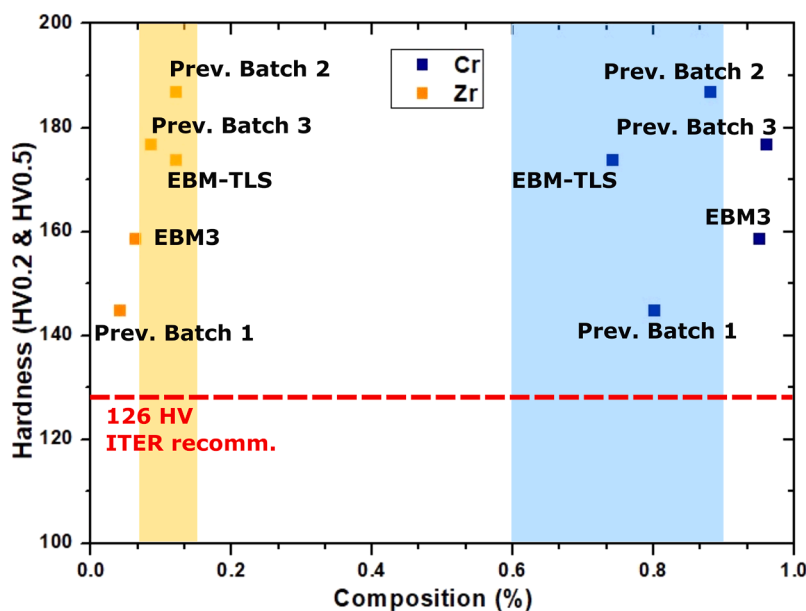


Fig. 22. Role of alloying elements (Cr and Zr) on hardness. Hardness values obtained from previously EB-PBF-manufactured batches [31] are included. The minimum hardness value recommended for ITER for the Solution Annealed and Aged CuCrZr-ITER Grade is also indicated (126 HV) [41].

(HIP) treatment. Unlike conventional powder metallurgy where HIP processes require encapsulating the raw material, in additive manufacturing, the final-shaped part can be directly subjected to HIP. This is feasible as long as there are no surface pores interconnected with the interior of the material, which could otherwise destabilize the process. This advantage significantly simplifies the HIP treatment in AM, making it a more practical and efficient option for producing complex geometries. The nature of the inner pores allowed for this improvement achieved in the relative density values after HIP, as spherical and non-interconnected internal pores were obtained from the EB-PBF process. These characteristics were crucial for reducing porosity values via the HIP treatment. In addition, HIP also seems to act as a conventional ageing treatment, promoting the precipitation of residual Cr that may remain in solid solution within the Cu matrix after the EB-PBF process. However, further in-depth TEM investigations are recommended to confirm the increase in density of Cr-rich precipitates. The promising thermal conductivity results obtained from the densified specimens align well with the desired thermal performance criteria for High Heat Flux components, underscoring the importance of mitigating porosity to ensure effective performance.

The microstructure of both the as-built and the HIPped specimens showed elongated zigzag Cu grains, aligned parallel to the building direction. This microstructure has been previously reported in other PBF additive manufacturing technologies and it was associated with the scan patterns procedures employed between each layer printed during the EB-PBF process. Conventional grains and grain boundaries coexist with solidification-enabled cellular-like subgrains and a homogeneous distribution of ultra-fine Cr-rich precipitates, obtaining a complex hierarchical microstructure which is responsible for the outstanding mechanical properties achieved. The presence of larger Zr-rich precipitates has been noted, presumably located at the limits of melt pools and grain boundaries.  $Zr_2O_3$  islands were also detected; however, in this case, they contribute to the weakening of the mechanical properties.

The role of Cr and Zr concentrations on the final mechanical properties was discussed, leading to the following conclusions: Zr plays a significant influence, potentially due to the grain refinement effect provided by Zr-rich precipitates located at the grain boundaries. In-depth TEM investigations are recommended to confirm this hypothesis. Additionally, Cr content also significantly influences the final mechanical properties. It has been demonstrated here that a slightly higher Cr content, exceeding the limit allowed by the ITER Grade of CuCrZr, does not result in the coarsening of Cr-rich precipitates. Instead, it achieves a homogeneous distribution of nanometric Cr-rich precipitates, with sizes ranging from several nanometers to 100 nm, even in the as-built condition. Consequently, future gas atomization and EB-PBF batches will aim for Zr contents close to the upper limit specified by the ITER Grade of CuCrZr to harness the benefits of this alloying element, while Cr concentration will be slightly above the permitted limit to further increase of mechanical properties. Nevertheless, careful attention must be paid to the O content to prevent the formation of detrimental  $Zr_2O_3$  islands, which could compromise the final mechanical properties.

Mechanical characterization has revealed excellent tensile and hardening properties comparable to, and in some cases surpassing, those of conventionally manufactured CuCrZr and those obtained by other additive manufacturing technique. As mentioned earlier, these exceptional mechanical properties can be attributed to the hierarchical microstructure achieved through the EB-PBF. Notably, the mechanical results obtained demonstrate the feasibility of EB-PBF to produce CuCrZr components suitable for the nuclear fusion field. Additionally, the flexibility of AM to create complex geometries is ideal for manufacturing heat exchangers with intricate internal cooling channels and high surface-to-volume ratios. Am also reduces the need for welding operations, which can adversely affect the microstructure and mechanical properties, thereby ensuring the integrity and performance of the components.

## CRediT authorship contribution statement

**F. Canillas:** Writing – review & editing, Writing – original draft, Validation, Methodology, Investigation, Formal analysis, Data curation, Conceptualization. **E. Leon-Gutierrez:** Writing – review & editing, Supervision, Resources, Project administration, Methodology, Investigation, Funding acquisition, Formal analysis, Data curation, Conceptualization. **M. Roldan:** Writing – review & editing, Methodology, Formal analysis. **R. Hernandez:** Methodology, Formal analysis. **E. Urionabarrenetxea:** Methodology, Investigation, Formal analysis. **E. Cardozo:** Methodology, Formal analysis. **L. Portoles:** Methodology, Conceptualization. **J.R. Blasco:** Methodology, Conceptualization. **N. Ordas:** Writing – review & editing, Supervision, Investigation, Funding acquisition, Formal analysis, Conceptualization.

## Declaration of competing interest

The authors declare that they have no known competing financial interests or personal relationships that could have appeared to influence the work reported in this paper.

### References

## Data availability

Data will be made available on request.

## Acknowledgments

This work has been carried out within the framework of the EUROfusion Consortium, funded by the European Union via the Euratom Research and Training Programme (Grant Agreement No 101052200-EUROfusion). Views and opinions expressed are however those of the authors only and do not necessarily reflect those of the European Union or the European Commission. Neither the European Union nor the European Commission can be held responsible for them.

The work has also supported by the Grant TED2021-129825A-I00 funded by MICIU/AEI/ 10.13039/501100011033 and by the “European Union NextGenerationEU/PRTR.

## References

- [1] J.H. You, G. Mazzone, E. Visca, et al., Divertor of the European DEMO: engineering and technologies for power exhaust, *Fusion Eng. Des.* 175 (2022) 1130110, <https://doi.org/10.1016/j.fusengdes.2022.113010>.
- [2] Z. Vizvary, W. Arter, C. Bachmann, et al., European DEMO first wall shaping and limiters design and analysis status, *Fusion Eng. Des.* 158 (2020) 111676, <https://doi.org/10.1016/j.fusengdes.2020.111676>.
- [3] J.H. You, C. Bachmann, V.G. Belardi, et al., Limiters for DEMO wall protection: initial design concepts & technology options, *Fusion Eng. Des.* 174 (2022) 112988, <https://doi.org/10.1016/j.fusengdes.2021.112988>.
- [4] K. Zhang, E. Gaganidze, M. Gorley, Development of the material property handbook and database of CuCrZr, *Fusion Eng. Des.* 144 (2019) 148–153, <https://doi.org/10.1016/j.fusengdes.2019.04.094>.
- [5] ITER Material Property Handbook (2004). Chemical composition (ITER Document No. G74 MA16, File Code: ITER-AK02-1100).
- [6] J.W. Martin, *Micromechanisms in Particle-Hardened Alloys*, Cambridge University Press, 1980.
- [7] J.H. You, G. Mazzone, E. Visca, et al., Conceptual design studies for the European DEMO divertor: rationale and first results, *Fusion Eng. Des.* 109–111 (2016) 1598–1603, <https://doi.org/10.1016/j.fusengdes.2015.11.012>.
- [8] ITER Plant Description, Ch.13 Materials (2WZL72), 2024.
- [9] V. Barabash, A. Peacock, S. Fabritsiev, et al., Materials challenges for ITER—current status and future activities, *J. Nucl. Mater.* 367–370 (2007) 21–32, <https://doi.org/10.1016/j.jnucmat.2007.03.017>.
- [10] M. Li, M.A. Sokolov, S.J. Zinkle, Tensile and fracture toughness properties of neutron-irradiated CuCrZr, *J. Nucl. Mater.* 393 (2009) 36–46, <https://doi.org/10.1016/j.jnucmat.2009.05.003>.
- [11] Barabash, V., Ioki, K., Merola, M., Sannazzaro, G., & Taylor, N. (2010). Materials for the ITER vacuum vessel and in-vessel components—current status. Presented at the First joint ITER-IAEA Technical Meeting on “Analysis of ITER Materials and Technologies” (23–25 November 2010, Principality of Monaco) (Vol. 31).

- [12] J.Y. Park, J.S. Lee, B.K. Choi, B.G. Hong, Y.H. Jeong, Effect of cooling rate on mechanical properties of aged ITER-grade CuCrZr, *Fusion Eng. Des.* 83 (2008) 1503–1507, <https://doi.org/10.1016/j.fusengdes.2008.07.006>.
- [13] D.J. Chakrabarti, D.E. Laughlin, The Cr-Cu (chromium-copper) system, *Bull. Alloy Phase Diagr.* 5 (1) (1984) 59–68, <https://doi.org/10.1007/BF02868727>.
- [14] U. Holzwarth, M. Pisoni, R. Scholz, et al., On the recovery of the physical and mechanical properties of a CuCrZr alloy subjected to heat treatments simulating the thermal cycle of hot isostatic pressing, *J. Nucl. Mater.* 279 (2000) 19–30, [https://doi.org/10.1016/S0022-3115\(99\)00278-0](https://doi.org/10.1016/S0022-3115(99)00278-0).
- [15] A.D. Ivanov, A.K. Nikolaev, G.M. Kalinin, M.E. Rodin, Effect of heat treatments on the properties of CuCrZr alloys, *J. Nucl. Mater.* 307–311 (2022) 673–676, [https://doi.org/10.1016/S0022-3115\(02\)01110-8](https://doi.org/10.1016/S0022-3115(02)01110-8).
- [16] Appendix A to Structural Design Criteria for ITER In-vessel Components (SDC-IC) (2013) (ITER Document No. G74 MA 8 01-05-28 W 0.2).
- [17] A. Bhattacharya, S. Zinkle, J. Henry, et al., Irradiation damage concurrent challenges with RAFM and ODS steels for fusion reactor first-wall/blanket: a review, *J. Phys. Energy* 4 (2022) 034003, <https://doi.org/10.1088/2515-7655/ac6f7f>.
- [18] F. Singer, C. Deisenroth, D.M. Hymas et al., Additively manufactured copper components and composite structures for thermal management, *Proceedings of the 16th IEEE Intersociety Conference on Thermal and Thermomechanical Phenomena in Electronic Systems (ITHERM)*, Orlando, FL, USA, 2017, pp. 174–183, [10.1109/ITHERM.2017.7992469](https://doi.org/10.1109/ITHERM.2017.7992469).
- [19] T.Q. Tran, A. Chinnappan, J.K.Y. Lee, et al., 3D printing of highly pure copper, *Metals* 9 (2019) 756, <https://doi.org/10.3390/met9070756>.
- [20] A. Durocher, D. Ayrault, Ch. Chagnot, M. Lipa, W. Saikaly, CuCrZr alloy hot cracking during electron beam welding, *J. Nucl. Mater.* 367–370 (2007) 1208–1212, <https://doi.org/10.1016/j.jnucmat.2007.03.220>. VolPart B.
- [21] S. Jaypuria, N. Doshi, D.K. Pratihari, Effects of welding parameters on mechanical properties in electron beam welded CuCrZr alloy plates, *IOP Conf. Ser. Mater. Sci. Eng.* 338 (2018) 012013, <https://doi.org/10.1088/1757-899X/338/1/012013>.
- [22] Y. Li, L. Jin, W. Zhu, et al., Vacuum joints of CuCrZr alloy for high-heat-load photon absorber, *J. Synchrotron Radiat.* 29 (2022) 363–368, <https://doi.org/10.1107/S160057752101273X>.
- [23] C. Wallis, B. Buchmayr, Effect of heat treatments on microstructure and properties of CuCrZr produced by laser-powder bed fusion, *Mater. Sci. Eng. A* 744 (2019) 215–223, <https://doi.org/10.1016/j.msea.2018.12.017>.
- [24] C. Salvan, L. Briottet, T. Baffie, L. Guetaz, C. Flament, CuCrZr alloy produced by laser powder bed fusion: microstructure, nanoscale strengthening mechanisms, electrical and mechanical properties, *Mater. Sci. Eng. A* 826 (2021) 141915, <https://doi.org/10.1016/j.msea.2021.141915>.
- [25] S. Uchida, T. Kimura, T. Nakamoto, et al., Microstructures and electrical and mechanical properties of Cu-Cr alloys fabricated by selective laser melting, *Mater. Des.* 175 (2019) 107815–107824, <https://doi.org/10.1016/j.matdes.2019.107815>.
- [26] K. Jahns, R. Bappert, P. Böhlke, U. Krupp, Additive manufacturing of CuCrZr by development of a gas atomization and laser powder bed fusion routine, *Int. J. Adv. Manuf. Technol.* 107 (2020) 2151–2161, <https://doi.org/10.1007/s00170-020-04941-7>.
- [27] Z. Hu, Z. Du, Z. Yang, L. Yu, Z. Ma, Preparation of Cu-Cr-Zr alloy by selective laser melting: role of scanning parameters on densification, microstructure and mechanical properties, *Mater. Sci. Eng. A* 836 (2022) 142740, <https://doi.org/10.1016/j.msea.2022.142740>.
- [28] Y. Sato, M. Tsukamoto, T. Shobu, et al., *In situ* X-ray observations of pure copper layer formation with blue direct diode lasers, *Appl. Surf. Sci.* 480 (2019) 861–867, <https://doi.org/10.1016/j.apsusc.2019.03.057>.
- [29] M.A. Lodes, R. Guschlbauer, C. Körner, Process development for the manufacturing of 99.94% pure copper via selective electron beam melting, *Mater. Lett.* 143 (2015) 298–301, <https://doi.org/10.1016/j.matlet.2014.12.105>.
- [30] R. Guschlbauer, S. Momeni, F. Osmanlic, C. Körner, Process development of 99.98% pure copper processed via selective electron beam melting and its mechanical and physical properties, *Mater. Charact.* 143 (2018) 163–170, <https://doi.org/10.1016/j.matchar.2018.04.009>.
- [31] N. Ordas, L. Portoles, M. Azpeleta, et al., Development of CuCrZr via Electron Beam Powder Bed Fusion (EB-PBF), *J. Nucl. Mater.* 548 (2021) 152841, <https://doi.org/10.1016/j.jnucmat.2021.152841>.
- [32] *Annual Book of ASTM Standards, Standard test method for density of powder metallurgy (PM) materials containing less than two percent porosity, designation B311-17*, 2017 vol. 02.05.
- [33] E. Smith, J. Nutting, Direct carbon replicas from metal surfaces, *Br. J. Appl. Phys.* 7 (1956) 214, <https://doi.org/10.1088/0508-3443/7/6/304>.
- [34] *Standard Test Methods for Tension Testing of Metallic Materials, Designation E8/E8M*, *Annual Book of ASTM Standards*, 2021 03.01.
- [35] *Annual Book of ASTM Standards, Standard Test Methods for Elevated Temperature Tension Tests of Metallic Materials, Designation E21-20*, 2020 03.01.
- [36] Z. Mao, D.Z. Zhang, J. Jiang, G. Fu, P. Zhang, Processing optimisation, mechanical properties and microstructural evolution during selective laser melting of Cu-15Sn high-tin bronze, *Mater. Sci. Eng. A* 721 (2018) 125–134, <https://doi.org/10.1016/j.msea.2018.02.051>.
- [37] Z. Ma, K. Zhang, Z. Ren, et al., Selective laser melting of CuCrZr copper alloy: parameter optimization, microstructure and mechanical properties, *J. Alloys Compd.* 828 (2020) 154350, <https://doi.org/10.1016/j.jallcom.2020.154350>.
- [38] Y. Bai, C. Zhao, Y. Zhang, J. Chen, H. Wang, Additively manufactured CuCrZr alloy: microstructure, mechanical properties and machinability, *Mater. Sci. Eng. A* 819 (2021) 141528, <https://doi.org/10.1016/j.msea.2021.141528>.
- [39] B.N. Singh, D.J. Edwards, M. Eldrup, P. Toft, Effects of heat treatments and neutron irradiation on microstructures and physical and mechanical properties of copper alloys, *J. Nucl. Mater.* 249 (1997) 1–16, [https://doi.org/10.1016/S0022-3115\(97\)00184-0](https://doi.org/10.1016/S0022-3115(97)00184-0).
- [40] K. Wang, K.F. Liu, J.B. Zhang, Microstructure and properties of aging CuCrZr alloy, *Rare Met.* 33 (2) (2014) 134–138, <https://doi.org/10.1007/s12598-014-0244-0>.
- [41] Z. Zhao, F. Li, Y. Chen, Y. Huang, Z. Wang, Joining of oxygen-free high-conductivity Cu to CuCrZr by direct diffusion bonding without using an interlayer at low temperature, *Fusion Eng. Des.* 151 (2020) 111400, <https://doi.org/10.1016/j.fusengdes.2019.111400>.
- [42] J. Sanz, C. González, J. Juan, Long-lived activity of elements: effect of new activation cross-sections and their uncertainties on the selection of materials for IFE reactors, *J. Nucl. Mater.* 258–263 (1998) 1700–1707, [https://doi.org/10.1016/S0022-3115\(98\)00155-X](https://doi.org/10.1016/S0022-3115(98)00155-X).
- [43] H. Helmer, A. Bauereiß, R.F. Singer, C. Körner, Grain structure evolution in Inconel 718 during selective electron beam melting, *Mater. Sci. Eng. A* 668 (2016) 180–187, <https://doi.org/10.1016/j.msea.2016.05.046>.
- [44] A. Rai, H. Helmer, C. Körner, Simulation of grain structure evolution during powder bed based additive manufacturing, *Addit. Manuf.* 13 (2017) 124–134, <https://doi.org/10.1016/j.addma.2016.10.007>.
- [45] Y.M. Wang, T. Voisin, J.T. McKeown, et al., Additively manufactured hierarchical stainless steels with high strength and ductility, *Nat. Mater.* 17 (2018) 63–73, <https://doi.org/10.1038/nmat5021>.
- [46] K.G. Prashanth, J. Eckert, Formation of metastable cellular microstructures in selective laser melted alloys, *J. Alloys Compd.* 707 (2017) 27–34, <https://doi.org/10.1016/j.jallcom.2016.12.209>.
- [47] Z. Chen, Y. Li, S. Zhang, et al., Hierarchical architecture and mechanical behavior of K418 Ni-based superalloys manufactured by laser powder bed fusion, *Mater. Sci. Eng. A* 851 (2022) 143630, <https://doi.org/10.1016/j.msea.2022.143630>.
- [48] D.A. Ramirez, L.E. Murr, E. Martínez, et al., Novel precipitate-microstructural architecture developed in the fabrication of solid copper components by additive manufacturing using electron beam melting, *Acta Mater.* 59 (2011), <https://doi.org/10.1016/j.actamat.2011.03.033>.
- [49] N. Ren, J. Li, R. Zhang, et al., Solute trapping and non-equilibrium microstructure during rapid solidification of additive manufacturing, *Nat. Commun.* 14 (2023) 7990, <https://doi.org/10.1038/s41467-023-43563-x>.
- [50] S.A. Fabritsiev, A.S. Pokrovsky, D.J. Edwards, S.J. Zinkle, The effect of neutron dose, irradiation and testing temperature on mechanical properties of copper alloys, *J. Nucl. Mater.* 258–263 (1998) 1015–1021, [https://doi.org/10.1016/S0022-3115\(98\)00389-4](https://doi.org/10.1016/S0022-3115(98)00389-4).
- [51] S. Tähtinen, M. Pyykkönen, P. Karjalainen-Roikonen, B.N. Singh, P. Toft, Effect of neutron irradiation on fracture toughness behaviour of copper alloys, *J. Nucl. Mater.* 258–263 (1998) 1010–1014, [https://doi.org/10.1016/S0022-3115\(98\)00075-0](https://doi.org/10.1016/S0022-3115(98)00075-0).
- [52] L. Li, Q. Wang, K. Wang, et al., Precipitation behaviour of supersaturated solid-solubility CuCrZr alloy by additive manufacturing, *Mater. Sci. Eng. A* 901 (2024) 146557, <https://doi.org/10.1016/j.msea.2024.146557>.
- [53] W. Zhou, T. Kousaka, S. Moriya, et al., Fabrication of a strong and ductile CuCrZr alloy using laser powder bed fusion, *Addit. Manuf. Lett.* 5 (2023) 100121, <https://doi.org/10.1016/j.addlet.2023.100121>.
- [54] V. Candela, L. Zanini, M. Tocci, et al., Influence of heat treatments on low-power-LPBFed CuCrZr for nuclear fusion applications, *J. Nucl. Mater.* 597 (2024) 155135, <https://doi.org/10.1016/j.jnucmat.2024.155135>.
- [55] J.Y. Park, Y.I. Jung, B.K. Choi, et al., Investigation on the microstructure and mechanical properties of CuCrZr after manufacturing thermal cycle for plasma facing component, *J. Nucl. Mater.* 417 (1–3) (2011) 916–919, <https://doi.org/10.1016/j.jnucmat.2010.12.157>.
- [56] ITER Document No. G74 MA16, ITER Material Properties Handbook, File Code: ITER-AK02-3112, 2004.
- [57] ITER Document No. S74 MA2, ITER Material Properties Handbook, File code: ITER-AK02-3112, 2004.